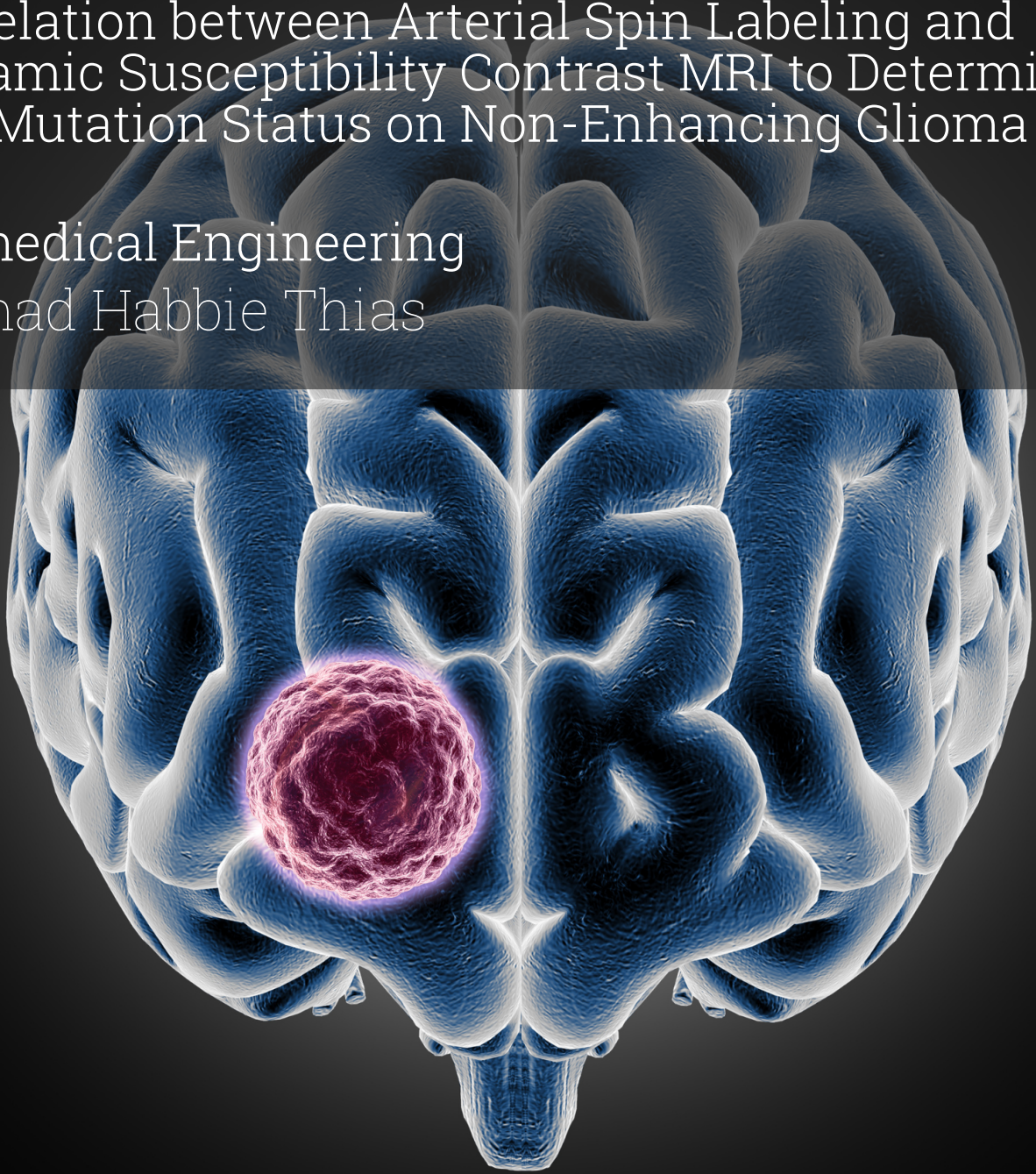# Master Thesis Report

Correlation between Arterial Spin Labeling and Dynamic Susceptibility Contrast MRI to Determine IDH Mutation Status on Non-Enhancing Glioma

Biomedical Engineering
Ahmad Habbie Thias

TUDelft

Erasmus MC
Universitair Medisch Centrum Rotterdam

Master Thesis Report

Correlation between Arterial Spin Labeling and Dynamic Susceptibility Contrast MRI to Determine
IDH Mutation Status on Non-Enhancing Glioma

by

Ahmad Habbie Thias

Student Number

5600510

to obtain the degree of

Master of Science in Biomedical Engineering Track Medical Physics at Delft University of Technology,

to be defended publicly on Wednesday, July 10, 2024, at 10.00.

Thesis Advisor I	: Prof. Juan A. Hernandez Tamames	TU Delft & Erasmus MC
Thesis Advisor II	: Dr. ir. Esther A.H. Warnert	Erasmus MC
Thesis Committee, Chair	: Dr. Frans M. Vos	TU Delft
Project Duration	: 11, 2023 - 06, 2024	
Faculty	: Faculty of Mechanical Engineering, Delft	

Cover: Brain Tumor by kjpargeter on Freepik
Style: TU Delft Report Style, with modifications by Daan Zwaneveld

TUDelft

Preface

This thesis was motivated by the need for non-invasive methods to accurately characterize gliomas, among the most aggressive forms of brain tumors. One of the biomarkers in glioma classification is the IDH mutation status. The glioma with the mutation in IDH (IDH-mutant) will have a better prognosis than the IDH-wildtype counterpart. Currently, the golden standard for diagnosing gliomas is taking biopsies and analyzing both histological and molecular features. In this thesis project, we propose an image processing technique combining perfusion MRI: Arterial Spin Labelling (ASL) and Dynamic Susceptibility Contrast (DSC) to distinguish IDH-mutant from IDH-wildtype.

Throughout this thesis, I have received invaluable support and guidance. I express my deepest gratitude to my supervisors, Prof. Juan A. Hernandez Tamames and Dr. Esther A. H. Warnert. Despite their busy schedules, they always made time for discussions, providing expertise, encouragement, and constructive feedback that were invaluable and kept me on the right path.

I also want to thank the iGene study team and the participating patients. Their contributions provided the data essential for this research. My colleagues and the technical staff at Delft's Faculty of Mechanical Engineering and Biomedical Engineering have also been incredibly supportive, offering assistance and collaboration whenever needed. A special thanks goes to my friends at Flex Desk Na2517 at Erasmus MC. They gave me a sense of home and community, offering invaluable feedback and stimulating discussions that significantly improved my thesis project.

My deepest gratitude goes to my family and friends. Their unwavering support and belief in me provided the motivation and strength to see this project through.

Completing this thesis has been both challenging and rewarding. I hope the findings of this research will inspire further studies and advancements in medical imaging and glioma characterization.

Ahmad Habbie Thias
Delft, July 2024

Abstract

Background: Glioma is a type of brain, originating from glial cells that support nerve cells, such as astrocytes and dendrocytes. It varies in type and severity, often resulting in a low life expectancy due to its aggressive nature. Since the implementation of the 2016 WHO Central Nervous System tumor classification, Isocitrate Dehydrogenase (IDH) mutation status has been used as a marker to distinguish the severity of the gliomas. This research explores the correlation between Arterial Spin Labeling (ASL) and Dynamic Susceptibility Contrast (DSC) MRI techniques to determine IDH mutation status in non-enhancing gliomas.

Methods: This project used 34 iGene patient dataset. To overlay ASL to DSC, both images were registered to the FLAIR images as the registration reference. The statistical analysis was done by dividing the tumor region for both ASL and DSC into three areas: hypo-perfusion, iso-perfusion, and hyper-perfusion. Then, the images were flattened from 3D to 1D data and the statistical analysis was done with Spearman's correlation. The correlation between those three areas for two imaging techniques resulted in nine cases. To test the interclass significance, the Mann Whitney-U test was used.

Results: This project found a higher mismatch area between ASL-CBF and DSC-rCBV in the IDH-wildtype group compared to the IDH-mutant group. Additionally, the mismatch area in IDH-wildtype shows a lower Spearman's coefficient, suggesting different information captured by those two imaging techniques. It reveals significant findings that both ASL-CBF and DSC-rCBV can be valuable in distinguishing IDH mutation statuses, with notable differences in perfusion characteristics between IDH-mutant and IDH-wildtype gliomas.

Conclusion: Voxel-wise correlation between ASL-CBF and DSC-rCBV can be a potential marker to distinguish IDH-mutant from IDH-wildtype.

Keywords: Arterial Spin Labelling (ASL), Dynamic Susceptibility Contrast (DSC), Isocitrate Dehydrogenase (IDH), Gliomas, IDH-mutant, IDH-wildtype, Cerebral Blood Flow (CBF), Cerebral Blood Volume (CBV), Perfusion Imaging.

Contents

Nomenclature

Abbreviations

Abbreviation	Definition
IDH	Isocitrate Dehidrogenase
ASL	Arterial Spin Labeling
DSC	Dynamic Susceptibility Contrast
WM	White Matter
GM	Grey Matter
CSF	Cerebrospinal Fluid
CBF	Cerebral Blood Flow
CBV	Cerebral Blood Volume
rCBV	Relative Cerebral Blood Volume
MRI	Magnetic Resonance Imaging
NAWM	Normally Appearance White Matter
NAGM	Normally Appearance Grey Matter
ATT	Arterial Transit Time
EGFR	Epidermal Growth Factor Receptor
TCA	Tricarboxylic Acid
FLAIR	Fluid Attenuated Inversion Recovery
WHO	World Health Organization
TERT	Telomerase Reverse Transcriptase
RBC	Red Blood Cells
Hct	Hematocrit

Symbols

Symbol	Definition	Unit
$R_i(t)$	Precontrast Relaxation Rate	$[mM^-1.s^-1]$
$R_{io}(t)$	Postcontrast Relaxation Rate	$[mM^-1.s^-1]$
ρ	Density	$[g/ml]$
α	Flip Angle	[degree]
TE	Echo Time	[ms]
TR	Repetition Time	[ms]
CBV	Cerebral Blood Volume	$[mL/100g]$
CBF	Cerebral Blood Flow	$[mL/(100g.s)]$

1

Introduction

Gliomas are primary brain tumors arising from the glial cell, which provides synaptic contact and maintains neurons' signaling abilities [1]. They are very diffusely infiltrative tumors that can affect surrounding brain tissue. Different types of gliomas exist, including glioblastoma, oligodendroglioma, and astrocytoma. Glioblastoma is the most malignant type of glioma. Each type of glioma has different clinical behaviors. An accurate diagnosis of the glioma is essential to determine the optimal therapy for the patient and improve their quality of life.

The classification of glioma has been significantly influenced by the understanding of the genetic basis of tumorigenesis [1]. Since the first classification guidelines of brain tumors by the World Health Organization (WHO), there have been several updates and refinements to the classification criteria of glioma. The previous classification of WHO's Central Nervous System in 2016 included molecular information; that classification guideline incorporated IDH1 mutation and 1p/19q codeletion for the first time and split the glioblastoma type into IDH-wildtype and IDH-mutant subcategory [2]. In addition, the 2016 classification also required necrosis and/or microvascular proliferation to be present in the histopathological analysis of biopsies for the glioma to be identified as glioblastoma [2]. In contrast, the 2021 WHO's CNS tumor classification restricts the use of the term "glioblastoma" to diffusely infiltrative gliomas that are IDH-wildtype and exhibit specific histopathological findings or molecular alterations, such as TERT promoter mutation, EGFR amplification, and chromosome 7 gain and chromosome 10 loss (+7/-10) [3]–[5]. This new classification replaced the previous IDH-mutant glioblastoma with the novel astrocytoma, IDH-mutant, grade 4. In the latest classification of glioma by WHO, there are three main adult diffuse gliomas those are Oligodendroglioma with IDH mutation and 1p/19q codeletion, Astrocytoma with IDH mutation but without 1p/19q codeletion, and Glioblastoma without mutation, i.e. IDH-wildtype. Molecular information on IDH mutation status determines the prognosis of glioma patients [6].

Currently, the gold standard for the classification of glioma is being done by taking a biopsy from the tumor and analyzing both histopathological and molecular features, which requires brain surgery. For non-invasive brain tumor diagnosis, imaging modalities such as Magnetic Resonance Imaging (MRI) are increasingly showing potential. MRI typically involves standard techniques such as T1-weighted, T1-weighted post-contrast injection, T2-weighted, and Fluid-Attenuated Inversion Recovery (FLAIR), which are essential for visualizing different aspects of brain pathology.

Additionally, functional MRI methods such as perfusion imaging can be beneficial for non-invasively diagnosing the glioma classification. Perfusion imaging is a type of medical imaging that evaluates blood flow to tissues and organs. It helps understand the tumor's vascularization, which correlates to the different types of gliomas. For instance, in oligodendroglioma with highly monotonous tumor cells, the vasculature is characterized in histopathology as a "chicken wire" mesh [7]. In contrast, astrocytoma microvasculature more often displays the same as normal brain parenchyma [8]. The glioblastoma type significantly varies in size and shape (irregular) of vascular structures[8]. Techniques like arterial spin labeling (ASL) and dynamic susceptibility contrast (DSC) are perfusion imaging methods included in MRI for analyzing tumor vascularization [9].

Moreover, tumors can be categorized based on their reaction to contrast agents used in magnetic resonance imaging (MRI). Enhancing tumors are defined by the region with increased uptake of these agents, resulting in heightened contrast on T1-weighted MRI scans post-injection. This characteristic is often associated with more aggressive tumor behavior. Historically, the surgical removal of these contrast-enhancing sections has been linked to longer patient survival. Yet, glioma recurrence is common due to the tumor's tendency to spread beyond these visually distinct areas.

Non-enhancing tumors, in contrast, do not show contrast agent uptake; they were once considered to be predominantly low-grade or benign [10], often linked to IDH mutations (IDH mutant) that suggested a more favorable prognosis. Recent advances in molecular classification have challenged this perception, revealing that some non-enhancing gliomas, including certain high-grade astrocytomas and glioblastomas, can be highly malignant and aggressive, lacking contrast enhancement [11], [12]. This revelation underscores the critical need for accurate detection of IDH mutation status in non-enhancing gliomas to assess their potential malignancy and guide treatment strategies properly.

There is a notable lack of research focusing on non-enhancing gliomas. This research gap presents a significant challenge, as emerging evidence suggests a need for improved methods to detect and characterize the aggressive nature of certain non-enhancing gliomas. Accurately identifying the IDH mutation status in glioma can help clinicians determine the best treatment strategies.

This research is expected to determine the IDH mutation status in the brain tumor glioma by finding the correlation between ASL and DSC MRI images since both techniques provide information about the vascularization inside the tumor area. As previously explained, the IDH mutation status affects the classification of gliomas. The IDH mutation alters the tricarboxylic acid (TCA) cycle, slowing the tumor progression and resulting in less severe glioma[13]. Combining ASL and DSC MRI perfusion parameters might be useful in determining the vascularization that correlates to the IDH1 mutation status. The dataset for this project includes MRI images from patients with non-enhancing glioma recruited for the Imaging Genomics (iGENE) Study at the Erasmus MC. The dataset also included anatomical scans T1-weighted and T2-FLAIR and perfusion MRI techniques such as arterial spin labeling (ASL) and dynamic Susceptibility contrast (DSC).

<div align="right">

2

</div>

Theoretical Review

This chapter will explain the theoretical review related to the research questions. The first section will explain glioma, the changes in classification and grading criteria, and the role of IDH mutation status in classification and grading. The second section will explain different MR imaging techniques used to scan the anatomical or functional features of the brain.

2.1. Brain Tumor and Glioma

The classification of brain tumors is a crucial aspect of medical diagnosis and treatment. The World Health Organization (WHO) has introduced a classification system incorporating molecular parameters and histology to define various tumor entities, providing a structured approach for Central Nervous System (CNS) tumor diagnoses in the molecular era [1]. Brain tumors are commonly categorized as primary or secondary. Primary brain tumors originate at the site, while secondary tumors result from cancer spreading from other parts of the body [14]. Additionally, brain tumors can be classified based on their origin and growth, with different subtypes exhibiting differing biological behaviors [15]. Glioma is the most common primary brain tumor originating from glial cells.

2.1.1. The update of Glioma Classification

WHO published the latest tumor classification of the Central Nervous System (CNS). Since the fourth version of the WHO CNS tumor classification (2016), molecular information such as IDH mutation status has been included as the classification criteria. Previously, the classification of glioma relied only on the histology features. If the IDH mutation is present in a brain tumor, the tumor is considered less malignant than an IDH-wildtype tumor. Thus, the IDH mutation status of the tumor directly affects the patient's prognosis and therapy[13]. In this version, the adult diffuse glioma was classified as shown in figure 2.1.

Grade/ Origin	Astrocytic	Oligodendrial	Oligodendrial
I			
II	Low Grade Diffuse Astrocytoma	Low Grade Oligoastrocytoma	Low Grade Oligodendroglioma
III	Anaplastic Astrocytoma	Anaplastic Oligoastrocytoma	Anaplastic Oligodendroglioma
IV	Glioblastoma		

Figure 2.1: The classification for adult diffuse glioma based on WHO CNS 2016 Classification

The IDH mutation status is one of the main classification criteria for the WHO tumor CNS 2016. This classification can classify most oligodendroglioma and astrocytoma into IDH-mutant glioma and glioblastoma into IDH-wildtype glioma. The molecular information of 1p/19q codeleted (mutation with deletion of the short arm chromosome 1 and long arm chromosome 19) is also used to mark the presence of oligodendroglioma IDH mutant. Additionally, the ATRx (alpha-thalassemia/mental retardation, X-linked) loss and TP 53 gene (tumor suppressor gene) mutation are the molecular characteristics that can be used to classify the glioma as the astrocytoma IDH mutant. However, this molecular marker is not a compulsory classifier criterion. Furthermore, if IDH mutation status and 1p/19q codeletion status are not done, the glioma classification will fall under the NOS (not otherwise specified) class. The simplified graph for classifying adult diffuse glioma based on WHO tumor CNS classification 2016 is depicted by figure 2.2
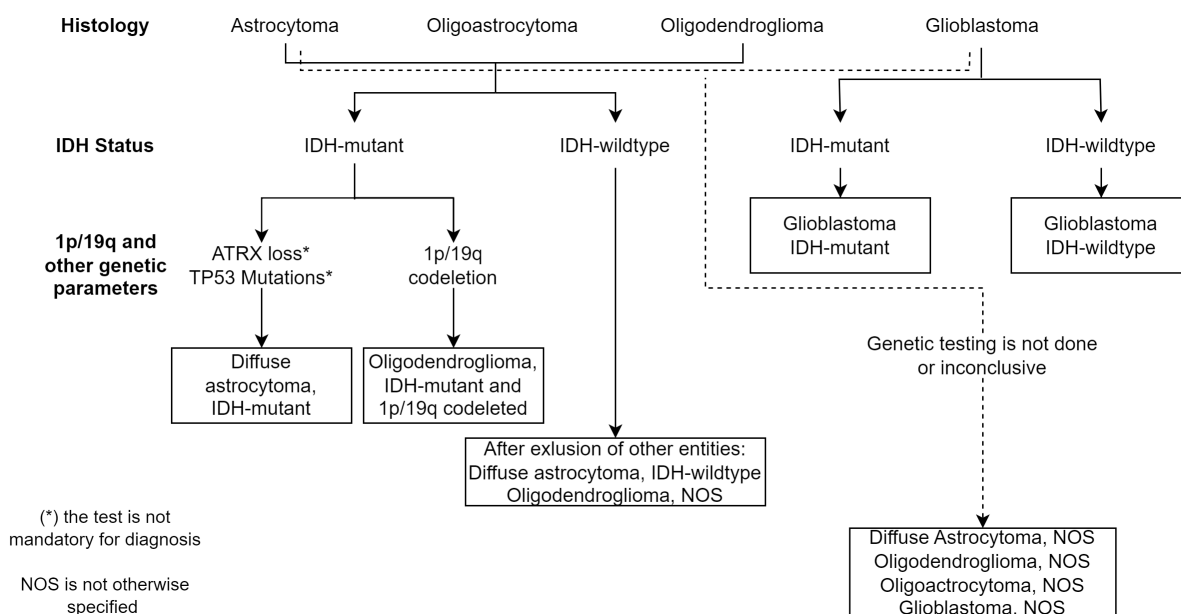

Figure 2.2: The classification for adult diffuse glioma based on WHO CNS 2016 Classification

The latest update in 2021 WHO CNS classification simplified the type of adult diffuse glioma into only three types:

1. Astrocytoma, IDH mutant (Grade 2,3,4).

2. Oligodendroglioma, IDH-mutant and 1p/19-codeleted (Grade 2,3).

3. Glioblastoma, IDH-wildtype(Grade 4).

The key different classification criteria of WHO Tumor CNS 2021 from WHO Tumor CNS 2016 are as follows.

1. Mixed glioma (oligoastrocytoma) is removed.

2. There is no glioblastoma IDH-mutant.

3. Anaplastic term is obsolete

4. Astrocytoma is always considered as IDH-mutant, even the grade 4 astrocytoma.

5. Addition of several molecular markers, such as TERT (telomerase reverse transcriptase) mutation, EGFR (epidermal growth factor receptor) amplification, or combined gain of entire chromosome 7 or loss of entire chromosome 10 [+7/-10] for the nonnecrotic or non-microvascular proliferative to be classified as glioblastoma.

6. Inclusion of CDKN2A/B homozygous deletion to classify glioma as astrocytoma grade 4.

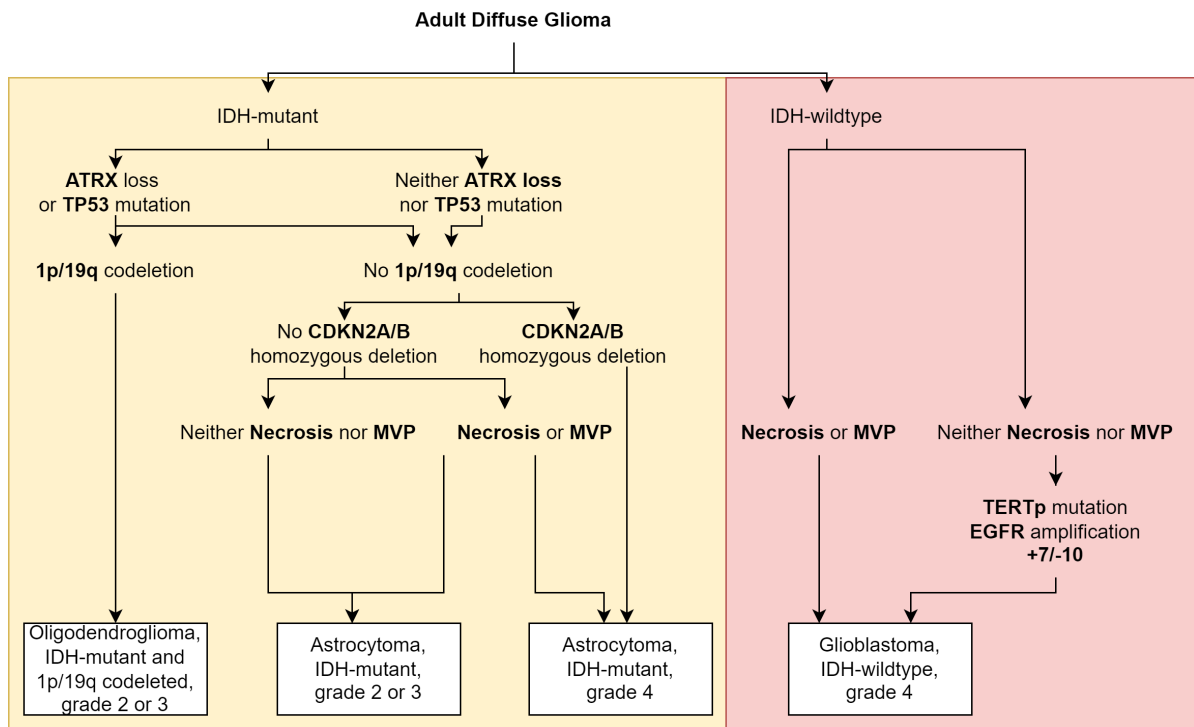The summary of adult diffuse glioma can be seen in figure 2.3.

Figure 2.3: The classification for adult diffuse glioma based on WHO CNS 2021 Classification. MVP is the acronym for microvascular proliferation. Modified from [16]

2.1.2. Glioma Histopathology

Before the incorporation of the 2016 WHO Tumor Classification for Central Nervous System (CNS), gliomas were classified only by using histology analysis of the tumor cell sample. The tumor samples are thinly sliced, stained, and examined under a microscope to reveal their morphological structure. Since tumor cells grow with abnormal molecular regulation, their morphological structure distinguishes them from normal cells.

There are three types of adult diffuse glioma in adult diffuse glioma: oligodendroglioma, astrocytoma, and glioblastoma. Each of those glioma types and their grading can be distinguished based on their morphological appearance. The tumor tissue morphology will be compared to the normal tissue. The astrocytoma comprises astrocytic cells with no cytoplasm and irregular hyperchromatic nuclei. Low-grade astrocytoma (IDH-mutant; Grade 2) appears to have a barely higher cell density, atypia, and low mitotic rate without increasing vascular density [17]. The progression toward higher grade (IDH-mutant; Grade 3) causes a higher cell density, atypia, and mitotic rate, with a mild increase in vascular density. For glioblastoma (IDH-wildtype; Grade 4), the cell density is increased, with pleomorphism, anaplasia, and an extreme change of microvascular hyperplasia [1,2]. Figure 2.4 shows different normal and tumor astrocytic histologies.
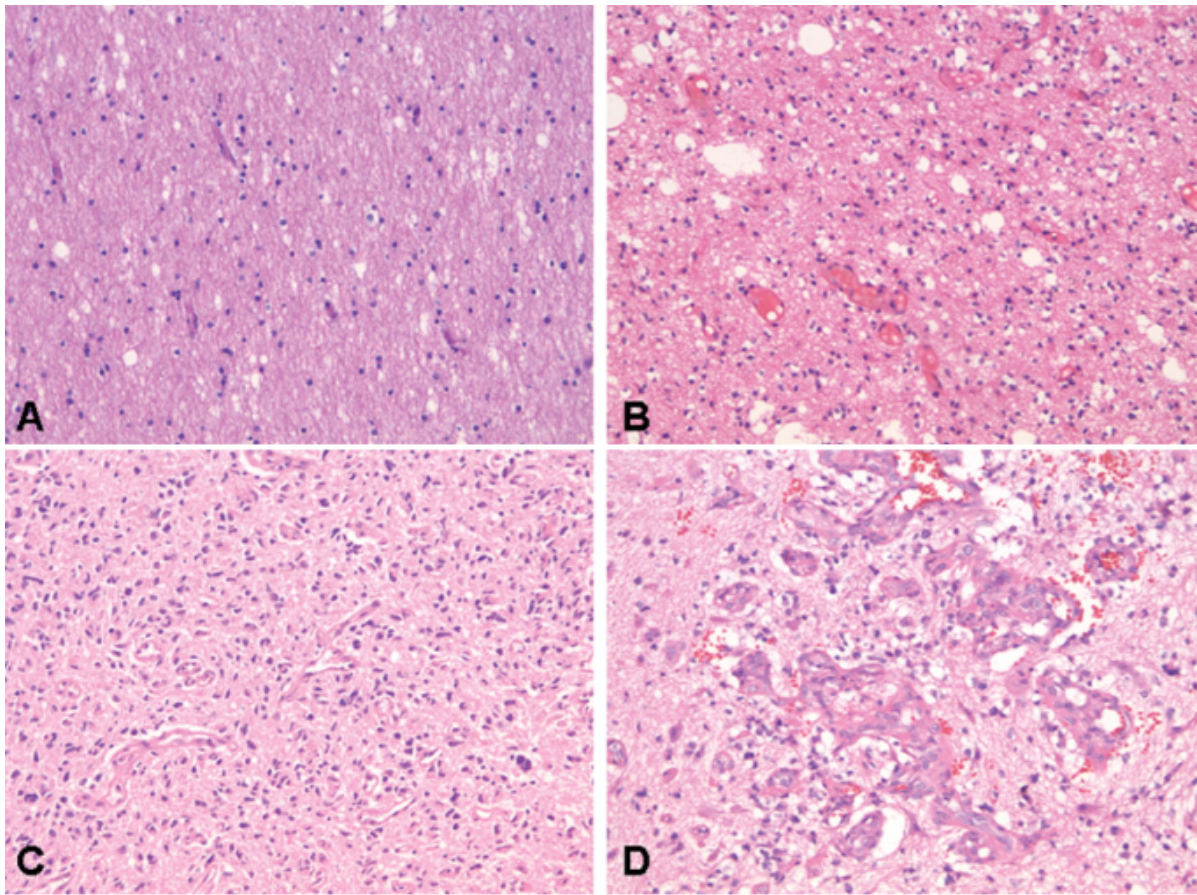
Figure 2.4: Astrocytic histology of (A) normal tissue; (B) Low-Grade Astrocytoma (IDH-mutant grade 2), the change in cell density is barely seen compared to normal tissue; (C) Astrocytoma (IDH-mutant grade 3), with higher cell density, atypia; (D) Glioblastoma, with an increasing cell density, pleomorphism, anaplasia, necrosis and/or glomeruloid microvascular proliferation [18]

In contrast to astrocytoma, the branching vasculature creates a distinguished "chicken-wire "pattern for the oligodendroglioma. This pattern causes an elevated cerebral blood volume (rCBV) in the dynamic susceptibility contrast due to increased vascularization[1]. Oligodendroglioma can be graded as grade 2 or 3, reflecting the level of tumor severity. Oligodendroglioma grade 3 appears as increasing cell density with nuclear anaplasia, high mitotic rate, microvascular proliferation, and/or necrosis [3]. Meanwhile, Oligodendroglioma grade 2 consists of cells with small to intermediate round, uniform nuclei [3]. Unlike astrocytic tumors, there is no grade 4 for this type.
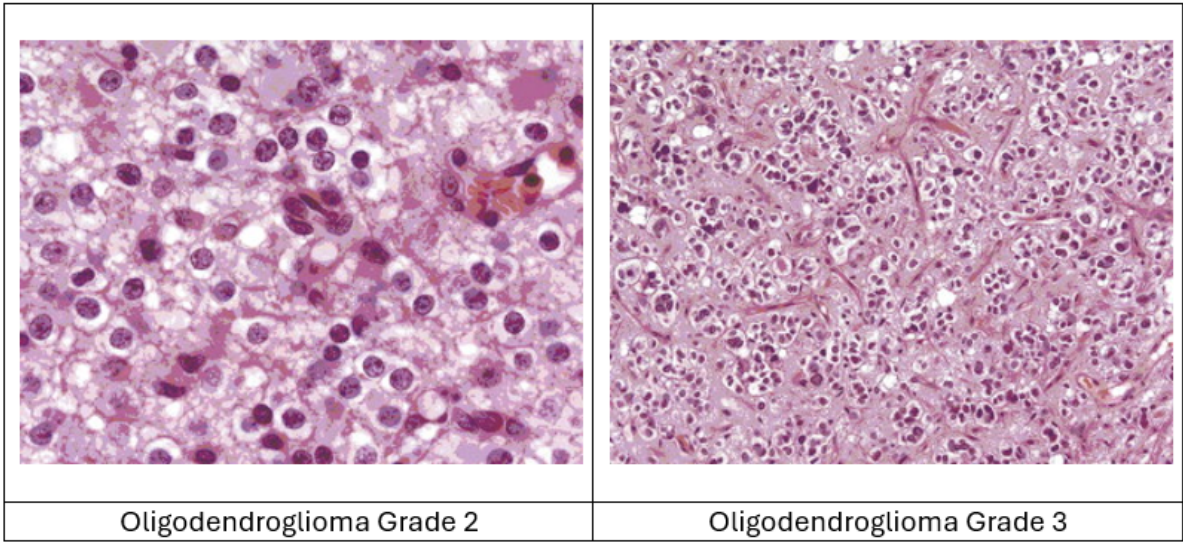
| Oligodendroglioma Grade 2 | Oligodendroglioma Grade 3 |

Figure 2.5: left panel: Oligodendroglioma grade 2, shown as monomorphic nuclei with perinuclear clearing (fried egg appearance); right panel: Oligodendroglioma grade 3, with increasing cell density, nuclear anaplasia, microvascular proliferation and branching vascular (chicken-wire like structure) [19]

In the past, the classification of adult diffuse glioma could be done solely based on histopathology features; however, in the current classification, molecular identification is needed to classify gliomas. Since the morphological features from histology cannot be quantified (e.g., there is no threshold for the mitotic level high or low), interobserver variability may occur. There are also some cases where an astrocytoma has an oligodendroglioma-like feature, which can cause mistakes in the classification. Thus, since 2016, the WHO classification of the central nervous system has included molecular analysis to distinguish different gliomas.

2.1.3. Gliomas' Molecular Features

As explained in the previous part, classifying gliomas solely based on histological features may cause a misclassification. This method is prone to inter-observer variability between pathologies. Thus, the inclusion of molecular features is essential for glioma classification.

One key molecular feature is IDH mutation status. Isocitrate dehydrogenase (IDH) participates in some metabolic processes, such as tricarboxylic acid cycle (TCA), glutamine metabolism, lipogenesis, and redox regulation [13]. IDH mutations in glioma cells produce a substance called D-2-hydroxyglutarate (D-2-HG) instead of the α-ketoglutarate (α-KG) as seen in figure 2.6. This substance disrupts the normal function of the TCA cycle, a key metabolic pathway that generates energy in cells. This disruption forces the cells to find alternative carbohydrate sources to sustain their energy and building material needs. One way the cells compensate is by increasing the use of glutamine, an amino acid converted to support energy production and other essential functions like lipid synthesis, especially under hypoxia.
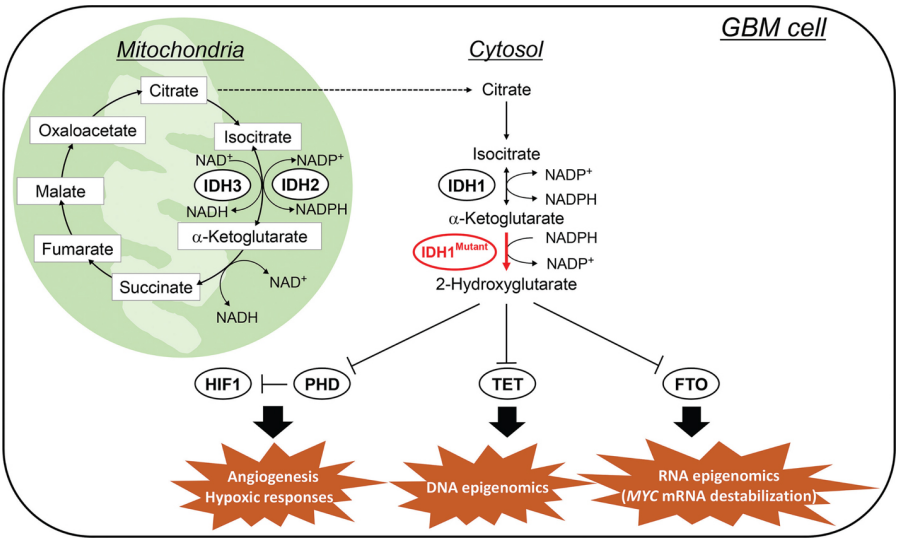
Figure 2.6: IDH1-mutant alter the Krebs cycle by reducing the α-KG into 2-HG [13]

Additionally, the presence of D-2-HG leads to widespread changes in how genes are regulated, primarily through hypermethylation. Hypermethylation affects several genes involved in glycolysis, effectively slowing down the glycolysis. This reduced activity in glycolysis is thought to contribute to the slower growth observed in IDH-mutant gliomas compared to IDH-wildtype [20].

Since the IDH mutation (IDH-mutant) slows the metabolism process in glioma, its presence indicates a better prognosis. In contrast, the absence of the IDH mutation (IDH-wildtype) shows the tumor's malignancy.

2.1.4. Imaging Features of Gliomas

Besides the golden standard practice of determining the classification and grading of gliomas with the biopsy analysis, some research unveils the capability of the imaging features to classify gliomas. One of the most common imaging modalities used to help the diagnosis is Magnetic resonance imaging (MRI), especially perfusion imaging. Dynamic susceptibility contrast (DSC) is commonly used in predicting glioma grading since it correlates well with angiographic vascularities [21]. Additionally, some research tries to quantify the cerebral blood volume (CBV) to distinguish low to high-grade gliomas [22], [23]. Furthermore, the research by Alafandi et al. [24] used intraoperative ultrasound to probe the vascularization and found that in glioblastoma, the microvascular structure are more heterogenous than both astrocytoma and oligodendroglioma, depicted by figure 2.7.
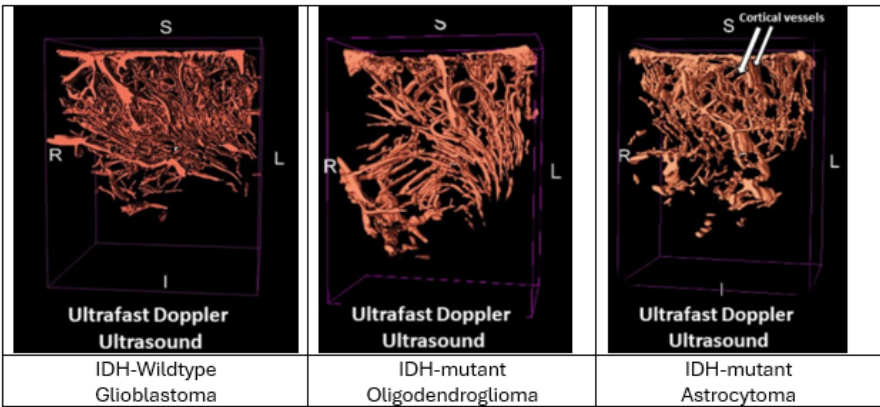

Figure 2.7: Research by Alafandi et al. [24] found that glioblastoma has a more heterogenous vascular structure than the other types of gliomas.

2.2. Magentic Resonance Imaging (MRI)

Magnetic Resonance Imaging (MRI) is an imaging device that employs magnetic fields and radio-frequency waves to noninvasively generate images of internal anatomy. Among the plethora of sequences available in MRI technology, T1-weighted, T2-weighted, and FLAIR (Fluid-Attenuated Inversion Recovery) sequences are particularly noteworthy for their distinct capacities to provide high-resolution anatomical structures for diagnosis.

T1-weighted imaging is useful in differentiating between fat and water content and visualizing soft tissue contrasts. This sequence excels in anatomical detailing, prominently featuring the cerebral gray and white matter, facilitating the precise mapping of brain structures. Conversely, T2-weighted imaging provides a complementary perspective with an enhanced sensitivity to fluid-containing tissues. Its ability to represent fluid-rich areas can help to identify pathological conditions characterized by edema, inflammation, or cystic formations, which may be less apparent on T1-weighted scans.

FLAIR imaging, a variant of the T2-weighted sequence, incorporates an inversion recovery pulse (very long echo and repetition time) to suppress the signal from free water, thereby making any abnormalities remain bright. Still, the normal CSF is attenuated and made dark. This feature is especially important in the case of non-enhancing tumors.

While T1, T2, and FLAIR MRI sequences provide insightful anatomical structures within the body, they fall short of showcasing the dynamic physiological processes crucial for tumor diagnosis, such as vascularization and blood flow. Recognizing the limitations of purely anatomical imaging, the focus shifts towards functional MRI techniques capable of capturing physiological information. The next part of the literature review will explain the perfusion imaging techniques with MRI.

2.3. Perfusion Imaging

Perfusion means the delivery of oxygen and other nutrients from the blood vessel to the tissue; it measures the exchange of blood between the vascular compartment and tissue and is quantified as a tissue-specific unit (mL/g per minute). Clinically, in medical imaging, perfusion imaging refers to multiple qualitative and quantitative methods, such as blood flow, blood volume, and transit time.

Analyzing angiogenesis, the process through which new blood vessels form, is crucial in evaluating tumor progression and malignancy. Tumors often trigger angiogenesis as they grow rapidly, leading to hypoxia or oxygen deprivation when the oxygen demand outpaces the supply from existing vessels. In response, cancer cells, particularly cancer stem cells, form new, albeit imperfect, vasculature within the tumor mass. These emergent vessels are characterized by their immature structure, displaying increased permeability, inconsistent diameters, irregular branching patterns, and a size generally larger than normal vessels within the same tissue. To assess these angiogenic activities and their implications for tumor severity and classification, perfusion imaging techniques such as arterial spin labeling (ASL) and dynamic susceptibility contrast (DSC) MRI are employed. These MRI-based methods offer distinct approaches to capturing the environment of the blood flow and vessel permeability within tumors, providing insights into their vascular architecture and functionality. This project aims to delve into ASL and DSC to differentiate the IDH-mutant from IDH-wildtype in glioma.

2.3.1. Dynamic Susceptibility Contrast (DSC)

Dynamic susceptibility contrast (DSC) MRI is one of the most well-known methods for analyzing hemodynamics and vascularization of brain tissue. This technique requires the administration of a contrast agent, typically Gadolinium (Gd), to shorten the relaxation time of tissue water -mainly T2* - (in this case, blood), causing magnetic field inhomogeneities and leading to detectable changes in MRI signals[25]. The technique involves the injection of a contrast agent followed by rapid repeated imaging to capture the signal changes in the tissue over time. DSC-MRI is a valuable tool in clinical practice, especially for assessing high-grade gliomas and other brain pathologies.

The physics behind DSC-MRI involves the transient decrease in brain signal intensity after administering a contrast agent, which enables the computation of cerebral blood volume at the voxel level. The injection of the contrast agent influences dipole-dipole interaction, shortening T2 and T2* due to the susceptibility difference between the tissue's intra- and extravascular space that induces mesoscopic

magnetic field gradients. This phenomenon is studied using T2*-weighted gradient-echo sequences, which are sensitive to the susceptibility effects of the contrast agent. The technique exploits the loss of phase coherence of protons as they diffuse through spatially varying magnetic field gradients, leading to signal attenuation dependent on physiological and experimental factors. DSC-MRI has significant diagnostic value and is an essential tool in neuroimaging [26], [27]. The equation below defines the ability of the contrast agent to modulate the proton relaxation rate as the function of concentration; this equation is expressed in units of $mM^{-1}.s^{-1}$.

$$R_i(t) = r_i C_t(t) + R_{io} \tag{2.1}$$

Where i=1,2, and 2* denoting different relaxation rates; R_{io} and $R_i(t)$ are the pre- and postcontrast relaxation rates; $C_t(t)$ is the contrast agent concentration dynamic in the tissue; and r_i is the contrast agent's relaxivity.

DSC MRI can be acquired using gradient recoil-echo (GRE) and spin-echo (SE) pulse sequences. The simultaneous acquisition of GRE and SE DSC-MRI data allows for the advantages of each technique to be realized. Gradient echo DSC-MRI has an inherently higher signal-to-noise ratio (SNR) and sensitivity than spin echo DSC-MRI, resulting in larger signal changes with equal contrast agent doses or equal signal changes with lower contrast agent doses. On the other hand, SE DSC-MRI sensitivity peaks for capillary-sized vessels offer potential advantages for stroke microvascular imaging. The acquisition parameters for DSC-MRI, including pulse sequence, repetition time (TR), echo time (TE), flip angle, and temporal coverage, are important for optimizing the imaging technique. Generally, GRE-EPI (echo planar imaging) is recommended over SE-EPI for DSC-MRI, with specific TR, TE, and flip angle values tailored to the imaging environment and the desired sensitivity to contrast agent concentration and vessel size. The choice between GRE and SE DSC-MRI depends on the specific clinical or research application and the desired balance between sensitivity, SNR, and contrast agent dose[28].

Since this modality takes multiple scans through time, motion artifacts are some of the main problems for using DSC in clinical settings. A proper algorithm for image registration and motion artifact removal is essential to enhance the quality of the DSC image derivation. A commonly used post-processing tool for motion artifact correction and image registration is MC FLIRT (FMRIB's Linear Image Registration Tool, University of Oxford, Oxford, UK)[8].

The alteration of local inhomogeneity in patient blood provides the assessment of cerebral blood volume (CBV), cerebral blood flow (CBF), and mean transit time (MTT). The CBV is derived from the DSC MRI images and reflects the blood volume within a given tissue volume, providing information about microvascular density and angiogenesis. Research by Chakravoroty et al. revealed the potential of CBV parameters as a potential biomarker for characterizing tumor vascularity [29]. Additionally, longitudinal DSC-MRI has been explored for distinguishing tumor recurrence from pseudoprogression in high-grade gliomas, emphasizing the role of CBV in evaluating treatment response and disease progression [27].

CBF, another crucial perfusion parameter obtained from DSC-MRI, represents the volume of blood passing through a unit of tissue per unit of time, reflecting tissue perfusion and metabolic demand. Meanwhile, MTT, the mean transit time, is a perfusion parameter derived from DSC-MRI that reflects the average time taken for blood to pass through a given tissue volume. MTT provides valuable information about tissue perfusion dynamics and vascular characteristics, contributing to the comprehensive assessment of brain tumor perfusion.

In evaluating brain tumors, parameters beyond traditional perfusion and permeability metrics, such as vessel size, play a critical role in distinguishing tumor types. This is particularly relevant in detecting mutations like IDH, which are significant for tumor characterization. Research [8] delving into the vessel size within tumors has shed light on the microvascular architecture of three adult types of non-enhancing glioma, revealing that glioblastomas, for instance, exhibit a notably larger average vessel size compared to other forms.

It is essential to understand that acquiring accurate vessel size data necessitates a specific imaging approach; a single gradient-recalled echo (GRE) or spin-echo (SE) Dynamic Susceptibility Contrast (DSC) MRI acquisition is insufficient. Precise vessel size imaging requires integrating both GRE and SE DSC techniques to capture and analyze tumors' nuanced vascular characteristics accurately. This methodological consideration underscores the complexity of accurately assessing tumor angiogenesis

and highlights the importance of fully employing comprehensive imaging strategies to understand tumor vasculature.

The MR signal needs to be converted to estimate the perfusion parameters; the first step is to calculate the baseline of the MR signal intensity, S(0), before the contrast agent's arrival. This equation can estimate the MR signal as a function of time S(t) for single-shot GRE-EPI.

$$S(t) = M_0 \frac{\sin(\alpha)\left[1 - \exp\left(-TR \times R_1(t)\right)\right]}{1 - \cos(\alpha)\exp\left(-TR \times R_1(t)\right)} \exp\left(-TE \times R_2^*(t)\right) \tag{2.2}$$

M_0 is the equilibrium longitudinal magnetization; α is a flip angle; R_i is the relevant relaxation rate. While in single-echo GRE-EPI, the change of T2* relaxivity can be calculated as follows:

$$\Delta R_2^*(t) = R_2^*(t) - R_2^*(0) = \frac{1}{TE} \ln\left[\frac{S(t)}{S(0)} + \frac{E_1(0)}{E_1(t)}\right] \approx -\frac{1}{TE} \ln\left[\frac{S(t)}{S(0)}\right] \tag{2.3}$$

Commonly, the T1 effects (E_1) are negligible. In blood-brain barrier disruption (BBB), the acquisition is usually done with or without a pre-load bolus but with a low flip angle single GRE-EPI acquisition. Alternatively, special acquisitions, such as multi-echo, can be made. In the Dual-echo DSC MRI acquisition, the (E_1) is negligible; thus, the equation would be.

$$\Delta R_2^*(t) = R_2^*(t) - R_2^*(0) = \frac{1}{TE_1 - TE_2} \ln\left[\frac{S_{TE_1}(t)}{S_{TE_2}(t)} + \frac{S_{TE_1}(0)}{S_{TE_2}(0)}\right] \tag{2.4}$$

In the case of SAGE (Philips System) or HEPI (General Electric System) acquisition, the calculation of T2* relaxivity performs fitting of all five echoes.

$$\Delta R_2^*(t) = \frac{1}{TE_{SE} - TE_2} \left(\ln\left(\frac{S_{TE_{SE}}, \text{ pre}}{S_{TE_{SE}}(t)}\right) - \ln\left(\frac{S_{TE=0}, \text{ pre}}{S_{TE=0}(t)}\right)\right) \tag{2.5}$$

The DSC hemodynamic parameters are based on the dilution theory[30], which assumes that contrast agent concentration in a compartment model is uniform. Multiple functions derive the hemodynamic function. Firstly, the transport function $h(t)$ describes transit time distribution through the voxel and depends on vascular flow and structure. Then, the residue function $R(t)$ states the fraction of contrast agent present in the volume of interest after t time post bolus injection.

$$R(t) = \left[1 - \int_0^t h(\tau)d\tau\right] \Rightarrow h(t) = -\frac{dR(t)}{dt} \tag{2.6}$$

The third function is the arterial input function (AIF); clinically, different volumes of interest will have different C_{AIF}s due to varying sizes of blood vessel supplies. However, a single C_{AIF}, typically in the major cerebral artery, is employed practically. Semi- or fully automatic methods are normally used to determine the C_{AIF} based on multiple identification criteria [31].

Finally, the tissue contrast agent concentration-time curve- which reflects the contrast agent concentration in each voxel, can be obtained as a function of $C_{AIF}(t)$) and $R(t)$.

$$C_t(t) = \frac{\rho}{k_H} \cdot \text{CBF} \cdot \int_0^t C_{\text{AIF}}(\tau)R(t - \tau)dt \tag{2.7}$$

ρ is the density of brain tissue, and kH is the hematocrit factor. In practice, $C_t(t)$ and $C-_{AIF}(t)$ are derived from DSC-MRI data, and then the CBF can be obtained by deconvolution. The CBV can be approximated by taking the integral of the voxel-wise ΔR_2^* (rCBV = $\int_0^t \Delta R_2^* dt$) [32], for the BBB is intact. Then, the mean transit time can be acquired by calculating the ratio between CBV and CBF.

$$MTT = \frac{CBV}{CBF} \tag{2.8}$$

A challenge with DSC MRI is determining rCBV in the presence of leaky BBB. In regions with disrupted BBB, the contrast agent leaks into the extravascular space, reducing the calculation of rCBV. Thus, leakage correction is needed during post-processing to circumvent this issue.

Additionally, the perfusion value derived from a DSC MRI scan can be influenced by multiple factors, such as the main magnetic field strength, sequence type (gradient or spin echo), and physical condition (hematocrit, oxygen saturation). Research by Van Dorth et al [33] found that the relaxivity R_2^* increases with the field strength. Furthermore, their research also found that the R_2^* relaxivity is non-linearly increased with a higher hematocrit percentage for the DSC. This research finding shows that relaxivity is dependent on the hematocrit level. They also found that the hematocrit dependency is higher for the gradient echo sequences than the spin echo sequences.

2.3.2. Arterial Spin Labeling (ASL)

Arterial Spin Labeling (ASL) is a Magnetic Resonance Imaging (MRI) technique that quantifies blood flow to the brain using a completely non-invasive approach, distinct from other perfusion methods. ASL utilizes water molecules in the blood without requiring injected contrast agents as a natural tracer. The principle of ASL involves altering the magnetization of these water molecules in the major arteries feeding the brain. This alteration is achieved by applying an inversion pulse upstream of the imaging region. Following a brief delay, known as the post-labeling delay, an image is captured showing the inverted spins in the blood as it flows into the brain.

The idea behind this method is to alter the magnetization of the water molecule in the large artery that supplies blood flow to the brain. The blood flow tracer in basic ASL is provided by applying an inversion pulse proximal to the image region. Then, after a short delay (post-labeling delay), an image (labeled image) is acquired in the brain, which has an inverted spin in the blood. The signal can be improved by repeating the acquisition of controlled and labeled images. Meanwhile, the controlled image is acquired without any inversion of the water molecule spin in the blood. The signal readout between the controlled and labeled images will have an identical signal in any tissue other than the blood vessel and a different signal in the blood vessel due to the inversion in the large blood vessel. The difference between controlled and labeled images will result in only the signal from the inflowing blood [34]. imaging is significantly influenced by the T1 relaxation time of blood. T1 relaxation time, an inherent tissue property affecting signal intensity in MRI, is pivotal in ASL because it dictates how well the inverted spin signal can be maintained as blood flows into the brain. Figure 2.8 illustrates the basic principle of ASL.
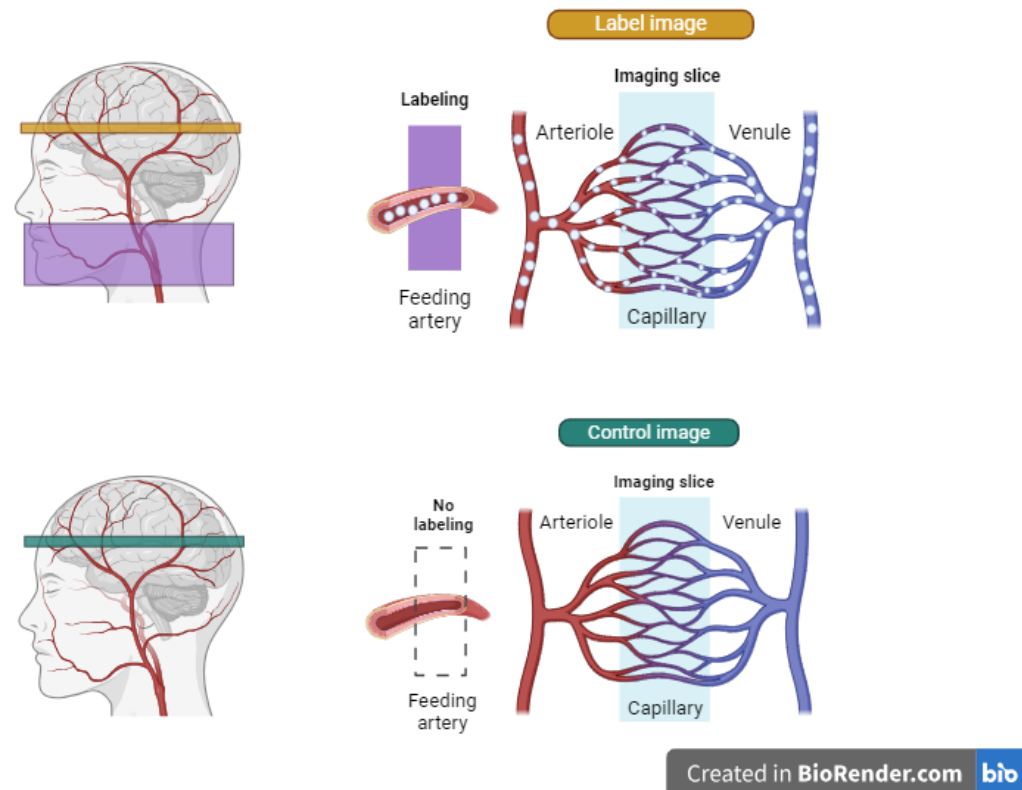
Figure 2.8: Illustration ASL basic principle, label image was acquired by inversing the water molecule spin inside the feeding artery. While the control image was taken without any spin inversion.

There are three different methods for labeling the blood water molecules in ASL: Pulsed ASL (PASL), continuous ASL (CASL), and pseudo-continuous ASL (pCASL). The advantages of PASL are a high labeling efficiency (98 %), low specific absorption ratio, and minimal magnetization transfer effect [7]. However, the other labeling technique has the lowest signal-to-noise ratio (SNR). On the other hand, CASL provides a slightly higher SNR than the PASL technique [35]. However, CASL has a higher SAR, magnetization effect, and lower tagging efficiency (80-95%) due to the flow velocity variations [35].

pCASL has the intermediate solution to take advantage of CASL's high SNR and PASL's higher tagging efficiency. Instead of using continuous or pulse radio frequency, this technique applies a train of discrete RF pulses with a length of 1-2ms for each pulse ms) with a gradient wave between two consecutive RF pulses, mimicking the flow-driven adiabatic in CASL. As a result, this technique has a labeling efficiency of 85% (between PASL and CASL) while having a higher SNR. This technique is currently preferred for clinical setup [36].

One issue in quantifying cerebral blood flow in the ASL is caused by the arterial transit time (ATT) variability. The ATT is the required time for the blood to flow from the labeling region to the image plane. ATT between patients can differ due to different ages, sexes, and pathological conditions. Commonly, ASL uses the single post-labeling delay (PLD), which assumes the entire tagged blood has arrived at the imaging plane after a single PLD. However, the PLD recommendation can differ between young and older subjects [5], where the older subject usually has a longer ATT, causing the CBF underestimation in distal and overestimation in the proximal region. The longer PLD can be applied to counter this issue but with a lower image quality due to label relaxation with blood T1. The ATT issue can be circumvented by applying multi-PLD. However, multi-PLD requires a longer acquisition time, causing the motion artifacts to lower the SNR.

Background suppression is recommended in the ASL because the blood signal only composes 0-3% of all tissue inside the imaging plane[37]. The background suppression can be done with an even number of nonselective 180-degree pulses affecting both blood and static tissue. The longitudinal

magnetization of the labeled blood ensures that it is not inverted with an even number of pulses. However, multi-PLD requires a longer acquisition time, potentially causing motion artifacts. The values of the ASL signal need to be calibrated with the arterial blood's equilibrium magnetization (M0). The recommended setup to acquire M0 requires a repetition time (TR) of 4-6 seconds.

The spatial resolution of the ASL technique is low compared to structural imaging; thus, for the regional analysis, the registration to a higher resolution anatomical image is required to understand the perfusion parameter fully. The rigid body registration is typically enough. The anatomical image is segmented into grey matter, white matter, and cerebrospinal fluid probability maps. Those probability maps can then be used for the ASL partial volume correction. The incorrect segmentation of the anatomical probability maps (usually in tumor tissue with an abnormal intensity that can fail the segmentation) can cause a wrong estimation of the CBF.

ASL's voxel size usually ranges between 2x2 and 4x4 squares in a plane with 4-8 mm thickness; this is larger than the thickness of grey matter (approximately 2.5mm), causing most ASL's voxel to contain a signal mixture of GM, WM, and CSF. Thus, the ASL voxel's value depends on the structural composition, referred to as the partial volume (PV) effect. One way to do PV correction is by downsampling the segmented structure of the higher-resolution image. The ATT differences between WM and GM can be used to improve the PV correction.

For the patient with glioma, ASL can be used for diagnosis, grading, and monitoring the tumor area. The tumor can exhibit hyperperfusion due to neovascularization. Some research has been done in studying the ASL capability in diagnosing and grading tumors, one comparing normal and tumorous tissue [38] in glioma. The analysis of the tumorigenesis of the glioma can also help to distinguish the severity of the glioma.

3

Research Objectives and Questions

This section will explain current research related to the project and the research question and objective.

Previously, the arterial spin labeling (ASL) technique was not clinically relevant due to the poor signal-to-noise ratio compared to the dynamic susceptibility contrast (DSC). However, DSC has some limitations, including the injection of gadolinium, which is not possible in patients with kidney issues. Many researchers are trying to correlate DSC to ASL images to determine if ASL can replace DSC, especially for glioma diagnosis. Research by Khashbat et al. [39] found that the ASL-CBF ratio correlated well with the DSC-rCBV ratio in the brain tumor; the statistical analysis for this research was done with the ratio of mean perfusion value in enhanced tumor ROI with the mean perfusion value in white matter area. Additionally, research by Lavrova et al. [40] identified 178 brain tumor lesions with both ASL-CBF and DSC-rCBV images and found that there are significant correlations between average tumor area ASL-CBF and DSC-rCBV, especially in the enhancing glioma cases. Another research by Hashido et al. [41] also observed a positive correlation between ASL-CBF and DSC-rCBF radiomic features in low-grade and high-grade contrast-enhancing glioma.

Current research mostly focuses on finding the correlation between ASL and DSC in contrast-enhancing tumors. Only one study [40] included non-contrast-enhancing tumors; however, the study included not only glioma but also other types of brain tumors. Previously, non-enhancing contrast tumor areas were considered less malignant; however, some research shows that glioblastoma (glioma with the worst prognosis) may appear as a non-enhancing tumor area [10], [42]. Thus, the non-enhancing tumor area should also be considered the region of interest for the tumor grading and classification.

Additionally, based on the literature study in this project, no research currently performs the correlation analysis between the perfusion value of ASL and DSC MRI to determine IDH mutation status. The IDH mutation status can be determined by performing a molecular analysis. The mutation status of IDH can help to determine the severity of glioma. However, this method required an invasive procedure to acquire a biopsy. Since perfusion imaging can show the delivery of blood into tissue, it may help to evaluate the vascular information related to the severity of glioma. Thus, the main research question of this master thesis project is described as follows.

**To what extent can correlation between DSC and ASL MRI distinguish
IDH mutation status in non-enhancing glioma?**

Since both ASL and DSC images have different fields of view and resolutions, it is important to find a way to combine them in the same map. So, in this project, some additional research questions were added to help answer the main research question.

1. Which registration method suites well to compare ASL and DSC?
2. How can the issue of different pixel sizes between ASL and DSC can be addressed?
3. How well do MRI-based perfusion values represent vascularization in glioma?

4

Materials and Methods

This chapter explains the systematic approaches and experimental procedures used to investigate the correlation between ASL, DSC, and Glioma's IDH mutation status. The materials subsection will define the image acquisition methods, the number of patients included, and a summary of the glioma classification of included patients. The methodology subsection will describe the image post-processing and statistical analysis methods.

4.1. Materials

4.1.1. Patients

The data were sourced from the iGENE study dataset, a comprehensive collection of information from 44 patients aged over 18 years. The iGENE study was specifically designed to evaluate the value of perfusion MRI for non-enhancing adult diffuse glioma diagnosis. All patients in this study provided written informed consent for their information to be stored and used for research purposes, and the Institutional Board Review of Erasmus MC approved this study. The scans were acquired one or two days before the tumor resection operation. The inclusion criteria for this study is only the patients with a posteriori confirmed glioma histopathologically. Additionally, only non-enhancing glioma patients were included, confirmed by experienced neuroradiologists pre- and postcontrast T1-weighted imaging visual inspection. Furthermore, molecular analysis is also done to verify the IDH mutation status. The gene study was initiated before the WHO 2021 classification criteria; however, histopathology and molecular analysis were sufficient to classify the dataset based on current WHO criteria. Of all 44 patients, 10 were excluded because of incomplete scan modalities (missing either ASL or DSC), poor image quality, or incomplete molecular information. The exclusion of these patients was necessary to ensure the reliability and validity of the study's findings. Therefore, only 34 patients were included in this research. The summary of patients included in this project can be seen in table 4.1.

Table 4.1: Overview of Patient Diagnosis in Dataset According to WHO tumor CNS 2021 Classification

Adult Diffuse Gliomas	IDH-Mutation Status	1p/19q-codeleted	Number of Patient
Astrocytoma	IDH-mutant	no	11
Oligodendroglioma	IDH-mutant	yes	16
Glioblastoma	IDH-wildtype	no	7
Patient with IDH-mutant			27
Patient with IDH-wildtype			7
Total Patients			34

4.1.2. MR Acquisition

The patients underwent 3T MRI scanning with a conventional brain tumor imaging protocol, extended with advanced imaging techniques. The image acquisition included 3D sagittal CUBE T2-weighted FLAIR (0.8x0.8 mm^2 in-plane resolution, slice thickness 1.6mm; TR/TE/TI= 6.1ms/2.1ms/1897ms), 3D spiral pseudo-continuous ASL with time-encoded labeling (seven effective label delays ranging from 0.8 to 2 s, with a reconstruction matrix of 128x128x42 and a resolution of 1.9x1.9x3.5mm^3), and 2D Hybrid Echo Planar Imaging (HEPI) with the configuration of GRE DSC (122 TRs, TR/TE 1500m/18.6ms, 15 slices of partial brain coverage over the tumor, slice thickness of 3 mm (with 1.0 mm gap between slices), voxel size: 1.875x1.875x4mm^3). A 7.5ml of gadolinium-based contrast agent (Gadovist, Bayer, Leverkusen, GE) was given during the DSC acquisition. The DSC acquisition was preceded by a preload bolus of equal size approximately 5 minutes before imaging. In addition, this study also included the T1-weighted scan (256x256x352 reconstruction matrix, resolution of 1x1x0.5mm^3; TR/TE=6.132ms/2.1ms) to determine contra-lateral grey matter for the normalization of both ASL and DSC perfusion matrix (will be explained more in the methods subsection.

4.2. Methodology

4.2.1. Image Processing

Perfusion Parameter Derivation

ASL-CBF was derived by the GE post-processing tool according to the method proposed in the study about multi-delay ASL [43]. Meanwhile, for the DSC image processing, if the motion artifact was detected (by manual inspection), then motion correction was performed with MC FLIRT (FMRIB's Linear Image Registration Tool, University of Oxford, Oxford, UK). Then, DSC-rCBV maps were calculated with the in-house Python software (version 3.11) designed by Arzanfaroosh et al[8]. In summary, the algorithm converts the GRE signal-time curve to a transverse relaxation rate of ΔR_2^* with equation 4.1:

$$\Delta R_2^*(t) = -(1/TE_{GRE}) \times (\ln(S_{GRE}(t)/S_{GRE}(0))) \tag{4.1}$$

where TE is the echo time; $S_{GRE}(0)$ and $S_{GRE}(t)$ are the time curve of the signal of GRE before and after gadolinium injection. Then the CBV can be calculated by performing the integration of transverse relaxation rate (R_2^*) in the time interval between time entrance (t_0) and exit time (t_1) of the gadolinium, as shown in equation 4.2.

$$CBV = \int_{t_0}^{t_1} \Delta R_2^*(t)dt \tag{4.2}$$

No leakage correction was employed for the GRE-rCBV calculation in this study due to no or very little contrast agent leakage since the tumors are not enhancing [8].

This project only compared ASL-CBF with DSC-rCBV since other research comparing ASL and DSC concluded that they are strongly correlated.

Tumor Region Segmentation

The in-house python "Glioseg" automatic segmentation implemented the tumor segmentation method by employing T1, T2, and FLAIR [8]. Those three scans were then resampled and registered into MNI ICBM 152 non-linear symmetric atlas version 2009a, with ITK-elastic (version 0.15.0). Afterward, automatic tumor segmentation is performed for each imaging modality. Then, the segmentation from each modality is combined into one tumor segment. The output of this tumor segmentation is the NIFTI image, with three labels: 1 for edema, 2 for necrosis, and 3 for enhancing tumor (if any). This project defines the tumor area as a combination of those three regions.

Image Registration

All images underwent registration in two domains: M0-ASL and FLAIR. Due to the limited field of view, registration was not performed in the DSC. Additionally, registration was not done in the T1 domain since it doesn't provide hyperintensity like FLAIR images in the non-enhancing tumor area. The registration results were then qualitatively compared to choose which registration domain would be used throughout this project. The image registration process flow chart can be seen in picture 4.1.
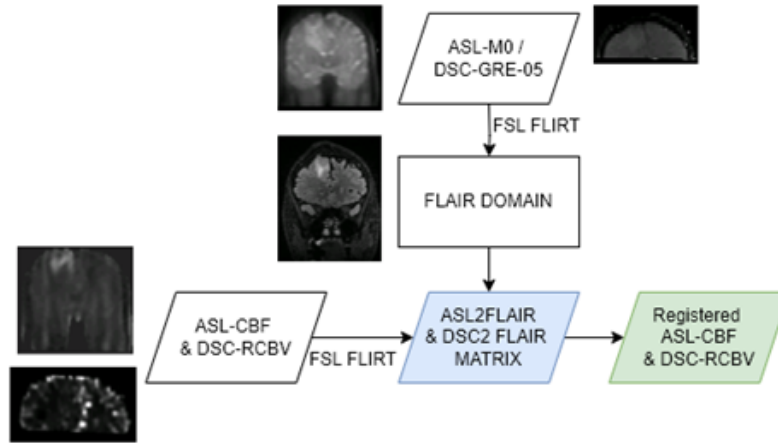
Figure 4.1: Flow Chart of Image Registration to FLAIR Domain

The four first-time volumes of DSC-GRE were removed to ensure the steady stated signal had reached [8]. M0-ASL is the perfusion calibration image for ASL. Both images were registered with the FSL linear registration (FLIRT version 6.0) with the FLAIR images as the anatomical references. The registration transformation matrixes were saved to register the derived perfusion matrix (ASL-CBF and DSC-rCBV) to FLAIR domain. In contrast, the registration to the M0-ASL domain can be seen in picture 4.2.
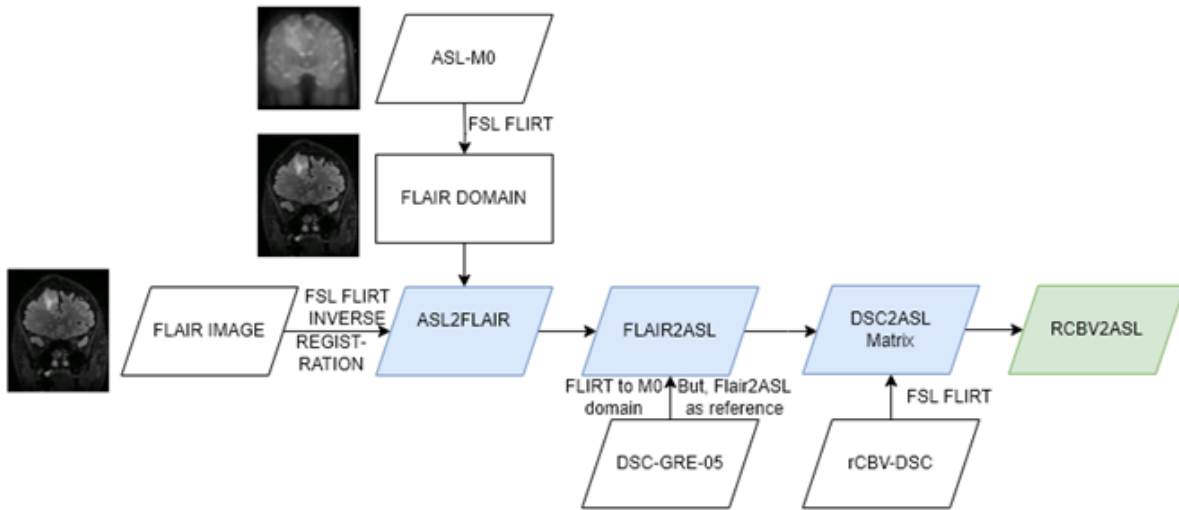

Figure 4.2: Flow Chart of Image Registration to M0-ASL Domain

Unlike the registration to the FLAIR domain, the registration to the M0-ASL domain has additional steps. The recommendation from FSL FLIRT documentation [44] stated that the registration from a higher resolution domain (FLAIR) to a lower resolution domain (M0-ASL) can be done by first registering the lower resolution image to a higher resolution image, and save the transformation matrix. Afterward, the higher resolution image can be registered to a lower registration image with the FSL FLIRT inverse registration function with a saved transformation matrix. Then, the FLAIR images in the M0-ASL domain will be the image reference to register DSC images.

Derived Perfusion Parameter Normalization
Since every patient has a different physiological characteristic, the derived perfusion parameter cannot be directly compared between each patient. For example, the hematocrit value can influence the DSC perfusion maps, so it is important to normalize all of the images to be compared for each patient without

any bias due to physiological differences. For DSC-rCBV, typically, normalization is done by dividing the DSC-rCBV by the mean intensity of normal appearance white matter (NAWM). NAWM represents the white matter area contralateral to the tumor region. Mathematically, the normalization of DSC can be formulated as equation 4.3.

$$nrCBV = rCBV/mean(NAWM) \tag{4.3}$$

However, since the ASL technique suffers from much lower SNR due to a long arterial transit time (ATT) and lower CBF value than grey matter [45], this project also normalized both perfusion values with normally appearing grey matter (NAGM). It should be noted that for the DSC-rCBV, normalizations are being done with NAWM, followed by NAGM. Meanwhile, the calculation is only done with the NAGM for the ASL-CBF. The equation for normalization with NAGM is shown in equation 4.4.

$$normalizedPerfusion = PerfusionValue/mean(NAGM) \tag{4.4}$$

NAWM and NAGM were generated by extracting WM and GM probability maps from the T1 image with FAST in FSL (FMRIB's Automated Segmentation Tool, Version 6.0.5) [46]. The probability maps were thresholded with 0.9 to minimize partial volume effects using FSLMATH with the kernel size of 3 x 3 x 3 mm^3 [8], resulting in an output of binary mask. Afterward, the contralateral to the tumor area was selected manually. The binary maps were registered together with ASL-CBF and DSC-rCBV. Then, the binary maps are multiplied with the ASL-CBF and DSC-rCBV to calculate the average intensity in the NAGM area. These averaging outputs were used to normalize the derived perfusion matrix. The flow chart of the normalization of NAGM can be seen in picture 4.3.
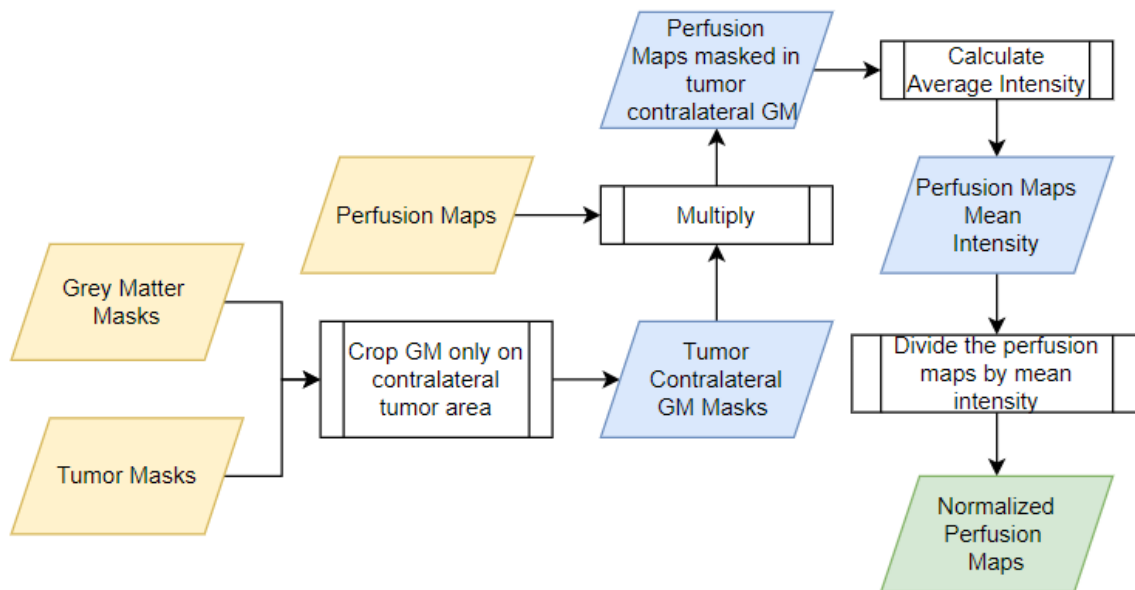

Figure 4.3: Flow Chart of Normalization with NAGM

4.2.2. Statistical Analysis

Statistical analysis were performed to check the correlation between ASL and DSC in distinguishing IDH mutation status in adult diffuse glioma. The study overlays the tumor ROI into the normalized perfusion matrix for the analysis. The perfusion histogram of one of the patients was plotted in Figure 4.4 to check the image intensity distribution.
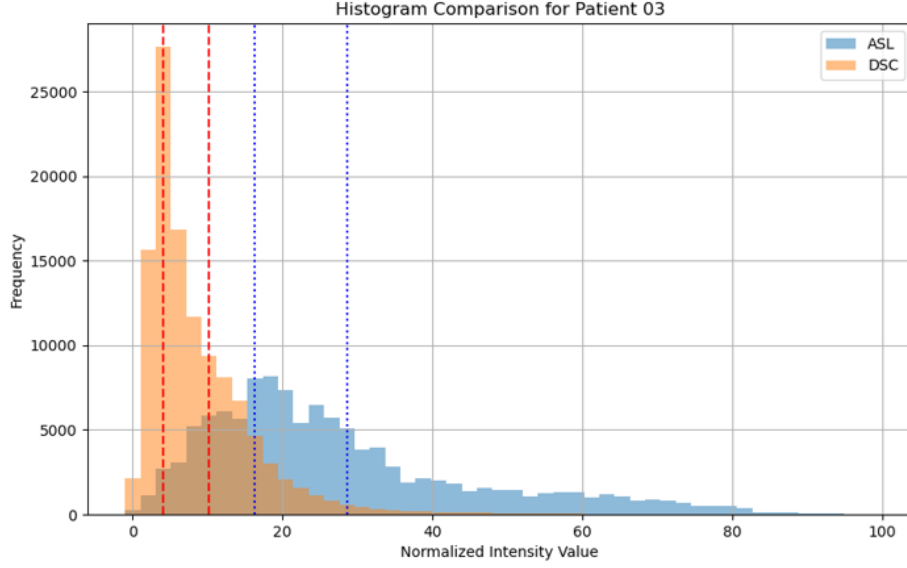
Figure 4.4: ASL-CBF and DSC-rCBV normalized histogram comparison inside tumor ROI

As seen in figure 4.4, ASL-CBF and DSC-rCBV have non-normal distribution histograms. Thus, the statistical methods employed in this project should account for the non-normal intensity distribution. In this project, the voxel-wise correlation between ASL-CBF and DSC-rCBV for each patient was performed using the Scipy Python package (version 1.12.0). Due to the non-normal distribution of these variables, the Spearman correlation coefficient was chosen for statistical analysis as it measures the strength of monotonic relationships without requiring normality. This method ranks the intensities in ASL and DSC, calculates the differences between these rank pairs, and determines the correlation. Firstly, this method will rank all the intensities in ASL and DSC. Then, the rank pairs (i) difference was calculated, resulting in d_i. In general, Spearman rank correlation was formulated as follows 4.5.

$$\rho = 1 - \frac{6 \sum d_i^2}{n \left(n^2 - 1 \right)} \tag{4.5}$$

where the n represents the number of data points. Unlike previous research, which correlated the mean of normalized ASL-CBF and DSC-rCBV, this approach may provide more insight into determining IDH mutation status. Before performing the voxel-wise correlation, both derived ASL-CBF and DSC-rCBV were flattened from 3D into 1D. Then, the flattened ASL-CBF and DSC-rCBV were inputted in the Spearman rank correlation. Spearman correlation rank value can be varied from -1 to 1. Which -1 represents a very strong negative correlation and vice versa. Generally, the strength of Spearman correlation can be verbally described in table 4.2.

Table 4.2: Spearman's Coefficient and Corresponding Strength Descriptions

Spearman's Coefficient	Description (Strength)
0.00-0.19	Very weak
0.20-0.39	Weak
0.40-0.59	Moderate
0.60-0.79	Strong
0.80-1.00	Very strong

In addition to examining correlations between ASL-CBF and DSC-rCBV within the tumor's ROI, this project categorizes ASL-CBF and DSC-rCBV intensities into three distinct zones: hyperperfusion (high

perfusion value), isoperfusion (medium perfusion value), and hypoperfusion (low perfusion value). By partitioning the ROI, this project aims to evaluate the overall correlation between ASL and DSC methodologies and analyze how different ASL-CBF and DSC-rCBV values relate. Each hyper-, hypo-, and isoperfusion represented in ASL-CBF and DSC-rCBV reflects unique physiological phenomena. DSC-rCBV measures the total amount of blood within a specific brain area. Meanwhile, ASL-CBF assesses the blood flow rate to different brain regions per minute. The three adult diffuse gliomas (glioblastoma, oligodendroglioma, and astrocytoma) have different blood vessel structures, which probably will cause different perfusion values in ASL-CBF and DSC-rCBV. By comparing these regions, the study seeks to gain insights into the potential of using perfusion MRI scans alone to distinguish IDH mutation statuses, thereby enhancing diagnostic precision in neuro-oncology. The correlation coefficients were calculated in 3^2 combination as shown in table 4.3.

Table 4.3: Perfusion Intensity Correlations between ASL-CBF and DSC-rCBV

	DSC-LOW	DSC-MED	DSC-HIGH
ASL-LOW	LL	LM	LH
ASL-MED	ML	MM	MH
ASL-HIGH	HL	HM	HH

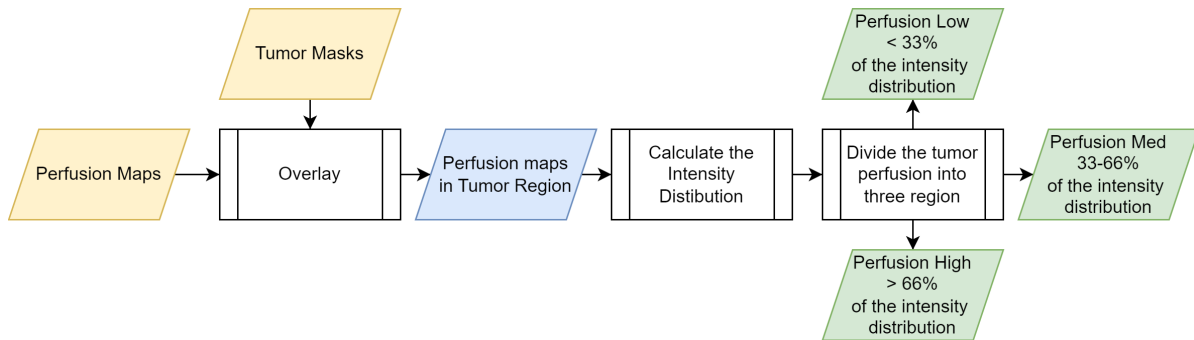The flow chart diagram for the correlation analysis can be seen in the figure4.5.

Figure 4.5: Intensity Thresholding Flowchart

The three regions of intensity were determined by calculating the overall intensity distribution. The hypoperfusion region has an intensity lower than 33 % of the whole tumor. Hyperperfusion is determined when a region contains an intensity larger than 66 % of the overall tumor. The isoperfusion is the region between hypo- and hyperperfusion. The overlapping area between different region combinations was also assessed to check how much overlap was in those combinations. The overlapping area was the ratio between the overlapping and whole tumor areas. The illustration of the overlapping area between ASL-CBF hyperintensity and DSC-rCBV hypointensity is shown in the figure below 4.6.
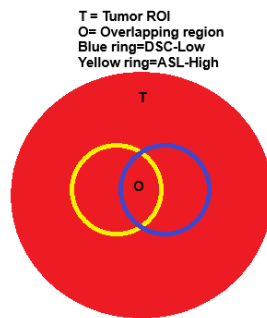

Figure 4.6: Illustration of overlapping ratio calculation

Then, the significant interclass test was done using the Mann-Whitney U Test. The non-parametric test was chosen since the data distribution is imbalanced between IDH-mutant(27 patients) and IDH-wildtype(7 patients). The P-value was considered significant when the value was lower than 0.05.

<div style="text-align: right;">

5

Results

</div>

This chapter presents the research results on the correlation between ASL-CBF and DSC-rCBV to distinguish IDH mutation status in adult diffuse glioma. The first section covers the registration results into two different domains: M0-ASL and FLAIR domain. Registration results analysis is important to ensure the research is reliable. The second section shows the generated grey matter masks to normalize both ASL-CBF and DSC-rCBV. In the third section, the correlation between the average ASL-CBF and DSC-rCBV intensity was provided to confirm the coherence of the dataset with the current research output (ASL-CBF and DSC-rCBV mean intensity are positively correlated). Then, the result will extended into the voxelwise correlation between ASL-CBF and DSC-rCBV as a whole tumor. The results of the overlapping area between different intensity regions are also provided. Finally, the last section provides the correlation analysis between different combinations of ASL-CBF and DSC-rCBV intensity regions.

5.1. Registration

The result of the registration of DSC-rCBV to the ASL domain is shown in the image below 5.1.

Figure 5.1: Overlay of DSC-rCBV on the FLAIR image that has been registered to the M0-ASL Domain

Performing the registration of the FLAIR image to a lower resolution makes the FLAIR image pixelated, which may influence the anatomical information in the patient's brain. Meanwhile, the registration of the DSC-rCBV to the FLAIR domain can be seen in figure 5.2

Figure 5.2 and 5.1 show that both registration results fit well with the FLAIR images. However, both image registrations show a dilated area near the skull, especially in the axial and frontal planes. This error was caused by the physical property of the GRE scan, which is sensitive to susceptibility differences, re-

Figure 5.2: Overlay of DSC-rCBV on the FLAIR domain

sulting in the susceptibility artifacts around the air and skull region, causing the distortion. Additionally, the registration of DSC-rCBV to the FLAIR domain resulted in smoother DSC-rCBV images compared to the registration to the M0-ASL domain.

5.2. Grey Matter Mask

As explained in Chapter 4, the Grey Matter mask was generated by measuring the grey matter probability maps from T1 scans. The GM maps were then thresholded with a value of 0.9 to generate binary masks. After generating the GM binary masks, the T1 was registered to the M0-ASL and FLAIR domains. The transformation matrix from T1 to the registration domain was used to register the binary mask to the registration domain. The GM mask registration in the M0-ASL and FLAIR domain can be seen in figure 5.3.
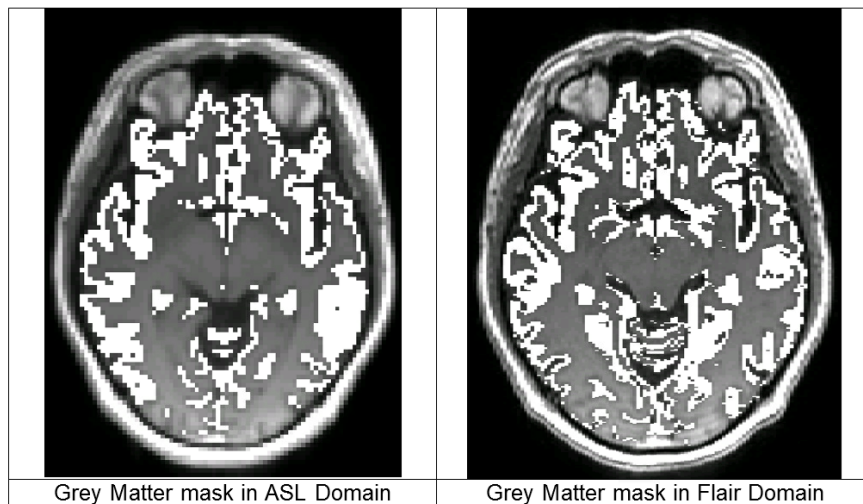

| Grey Matter mask in ASL Domain | Grey Matter mask in Flair Domain |

Figure 5.3: Grey Matter Masks Output from Different Registration Maps

From figure 5.3, the GM mask in the M0-ASL domain is more sensitive to contamination. The down-sampling of T1 to the M0-ASL threw away a lot of voxels to fit with lower-resolution images, distorting the anatomical information. The registration of T1 to the FLAIR domain, which has almost similar resolution, preserves the anatomical information, resulting in better GM mask registration results. Because of this, registration was done for the FLAIR domain for the rest of this project.

5.3. Whole Tumor Image Intensity

The average intensity inside the tumor area was calculated to compare ASL-CBF and DSC-rCBV values between different types of gliomas. The comparison between the ASL-CBF and DSC-rCBV values of each glioma can be seen in table 5.1.

Table 5.1: Mean of normalized DSC-rCBV and ASL-CBF Values inside Tumor Area for Different Glioma Types

Glioma Type	DSC-rCBV (mean ± std)[a.u.]	ASL-CBF (mean ± std)[a.u.]	IDH Mutation Status
Astrocytoma	0.4434 ± 0.0294	0.9353 ± 0.0514	IDH-mutant
Oligodendroglioma	0.6439 ± 0.2774	1.0274 ± 0.0759	IDH-mutant
Glioblastoma	0.6228 ± 0.1520	0.9662 ± 0.0633	IDH-wildtype

Table 5.1 shows that oligodendrogliomas have the highest average perfusion value for ASL-CBF and DSC-rCBV. Meanwhile, astrocytoma has the lowest average perfusion value for ASL-CBF and DSC-rCBV. The largest difference in average perfusion value can be seen in the DSC-rCBV, whereas for astrocytoma, the DSC-rCBV value is only 0.4434. At the same time, for both oligodendroglioma and glioblastoma, the DSC-rCBV value is around 30% higher. The visual representation of each glioma type can be seen in figure 5.4.
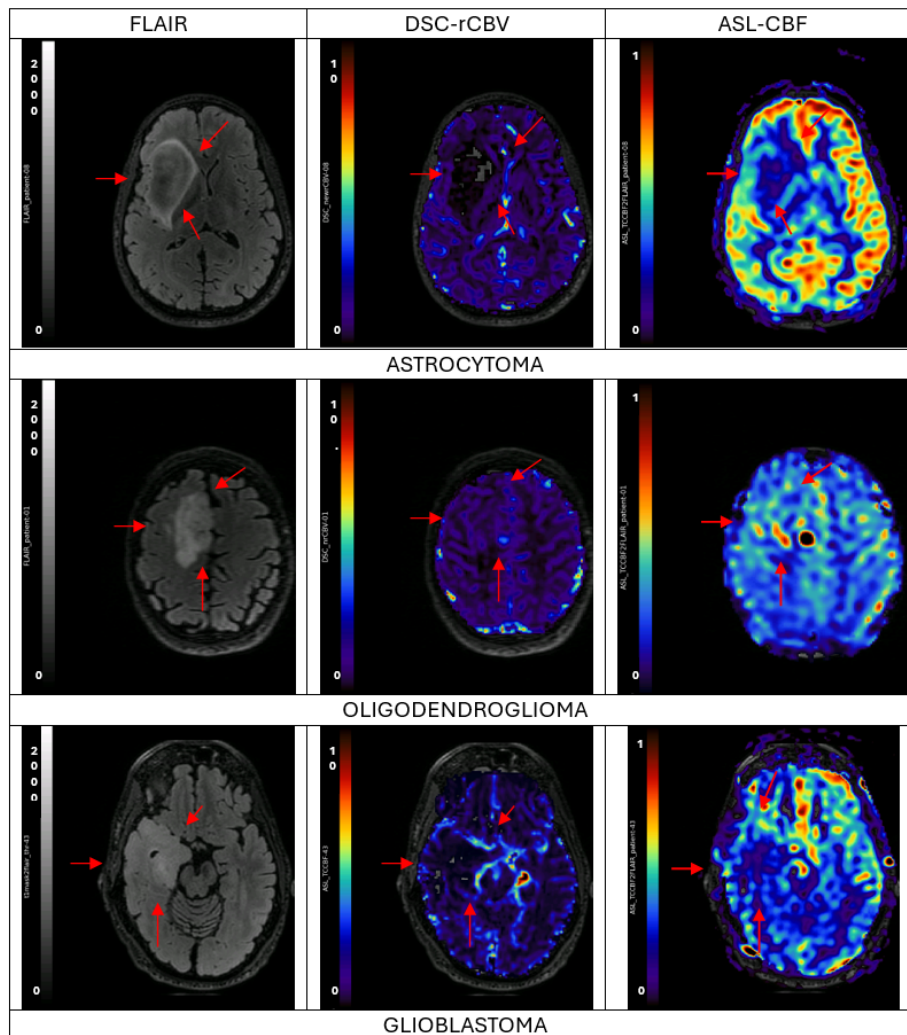

Figure 5.4: FLAIR, ASL, and DSC MRI appearance on different types of glioma, tumor areas are shown by the arrow

Figure 5.4 visually represents the MRI scan's appearance on various glioma types. The DSC-rCBV of

astrocytoma, for instance, is observed as a hypoperfusion region in contrast to its contralateral region. In contrast, the oligodendroglioma exhibits a hyperperfusion region within the tumor area, indicating distinct neovascularization compared to the contralateral tumor area. Conversely, glioblastoma manifests as a hypointensity of DSC-rCBV in the middle of the tumor ROI but with a hyperintensity in the rim of the tumor area. These visual features align with the quantitative value in table 5.1. Notably, the stark difference for ASL-CBF is only evident in the oligodendroglioma, which has an exceptionally high perfusion value within the tumor area. In contrast, the difference in ASL-CBF values between the tumor area and the normal contralateral region is more nuanced for both astrocytoma and glioblastoma.

5.4. Voxel-wise Correlation in Whole Tumor Region

The evaluation was done by performing a voxel-wise correlation between ASL-CBF and DSC-rCBV in the entire tumor area. This approach allowed for a comprehensive correlation analysis between the two perfusion parameters. These extensive tumor correlation results are presented in picture 5.5.
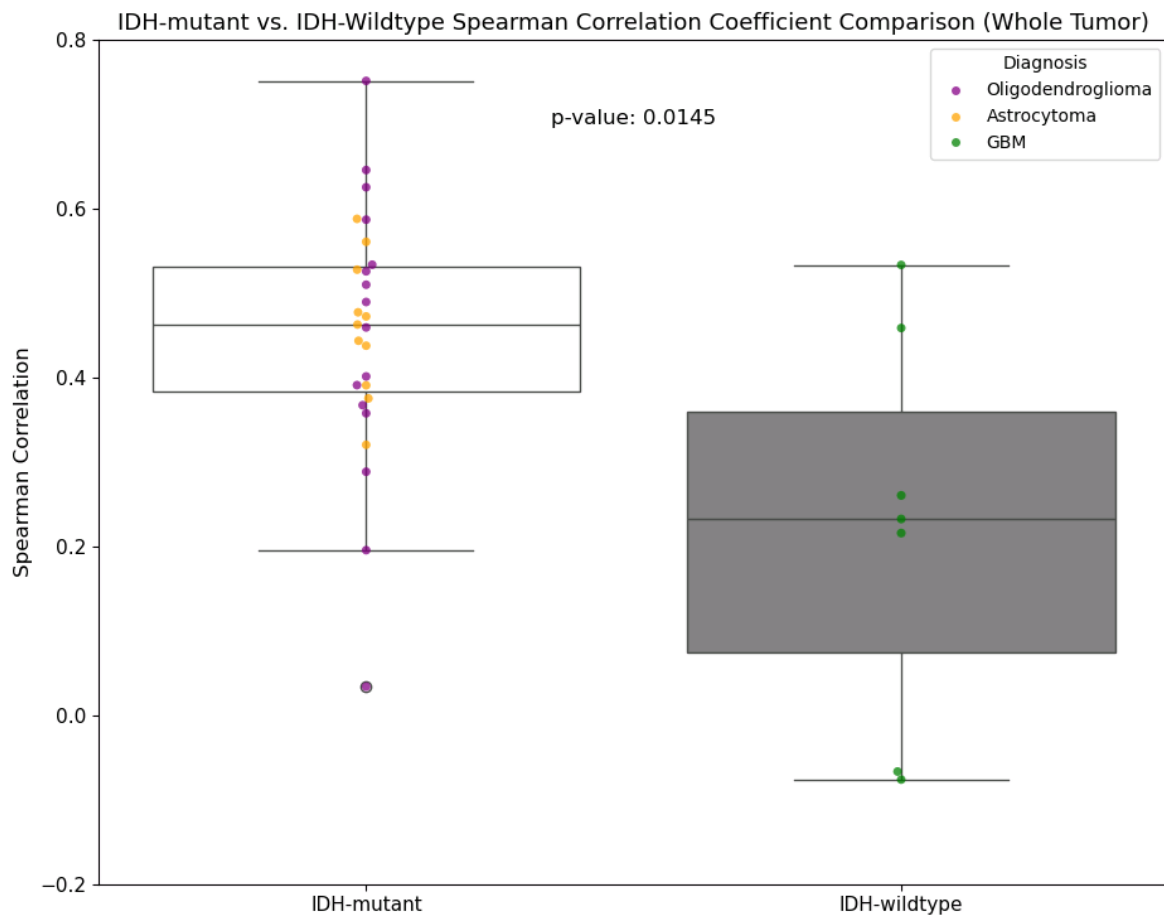

Figure 5.5: Boxplot of Voxelwise correlation (Spearmann Coefficient) between ASL-CBF and DSC-rCBV. The X-axis represents the different IDH mutation statuses, while the Y-axis represents the Spearman Correlation Coefficient.

The IDH-mutant case provides an average mild positive correlation between ASL-CBF and DSC-rCBV (mean Sperman's Coefficient=0.45). In contrast, the average IDH wildtype shows a weak correlation (mean Sperman's Coefficient=0.22) between the two perfusion parameters. The Mann-Whitney U test also showed statistical significance between two different mutation statuses. This result might indicate the voxel-wise correlation might be beneficial in determining the IDH mutation status with perfusion imaging.

5.5. Overlapping Area between Different Perdusion Region

Before comparing Spearman's correlation coefficient between ASL-CBF and DSC-rCBV between two groups of mutation status, this thesis project evaluated the overlapping area between different ASL-CBF and DSC-rCBV values.
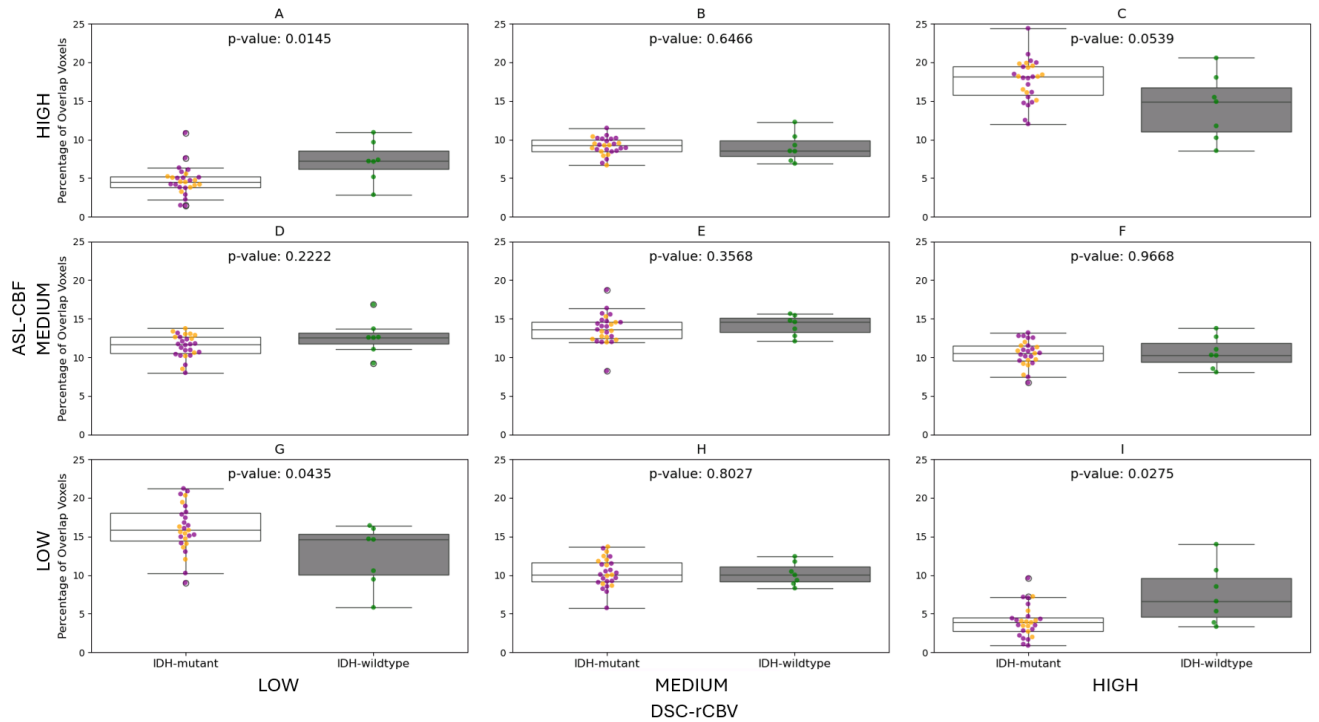

Figure 5.6: Overlapping region between ASL-CBF and DSC-rCBV different perfusion values. The boxplot's X-axis represents the different IDH mutation statuses, while the Y-axis represents the percentage of overlapping voxels.

Figure 5.6 illustrates the percentage of overlapping voxels between IDH-mutant and IDH-wildtype gliomas across different perfusion levels measured by ASL-CBF (Arterial Spin Labeling-Cerebral Blood Flow) and DSC-rCBV (Dynamic Susceptibility Contrast-relative Cerebral Blood Volume). The boxplots reveal that the same perfusion levels (C, E, G) generally exhibit higher overlapping areas compared to different perfusion levels (A, B, D, F, H, I). IDH-wildtype gliomas tend to have a lower overlapping area within the same perfusion intensity regions, indicating a higher mismatch between ASL-CBF and DSC-rCBV. Mismatch regions, where high and low perfusion levels overlap (A and I), are more common in IDH-wildtype gliomas. Statistical analysis shows that three cases are significant (p-value < 0.05) in distinguishing IDH mutation status: ASL-CBF Low and DSC-rCBV Low (G), ASL-CBF Low and DSC-rCBV High (A), and ASL-CBF High and DSC-rCBV Low (I). These findings suggest that IDH-wildtype gliomas exhibit more mismatched perfusion levels, aiding in the differentiation of IDH mutation status.

5.6. ASL-CBF and DSC-rCBV Voxelwise Correlation in Different Perfusion Intensity

This project also evaluated Spearman's correlation coefficient between different perfusion value regions of ASL-CBF and DSC-rCBV. The comparison between Spearman's correlation coefficient of IDH-mutant and IDH-wildtype is depicted in Figure 5.7.
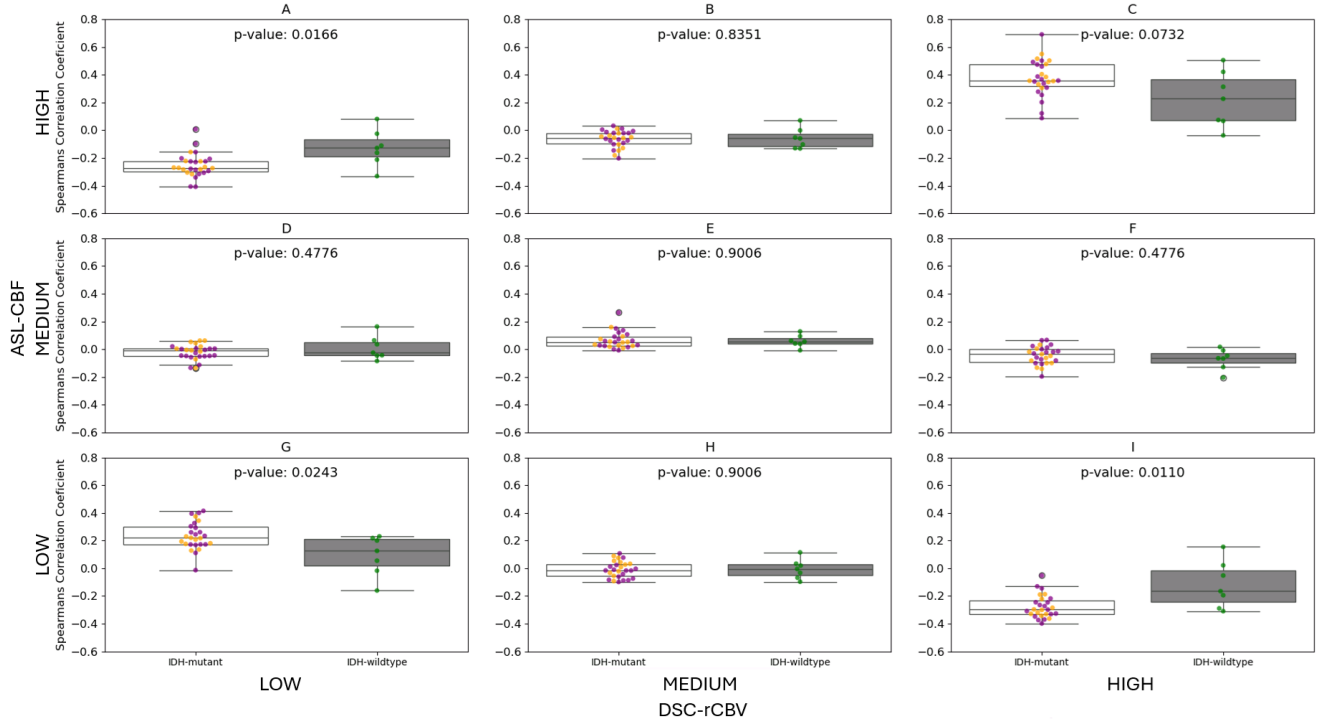

Figure 5.7: Voxelwise correlation between ASL-CBF and DSC-rCBV across different perfusion values. The boxplot's X-axis represents the different IDH mutation statuses, while the Y-axis represents the Spearman Correlation Coefficient.

In general, figure 5.7 shows that plots B, D, E, F, and H have a very small absolute Spearman's correlation coefficient for both IDH mutation statuses. Additionally, the statistical tests in those plots are insignificant (p-value > 0.05). In contrast, plots A, C, G, and I have a relatively larger absolute Spearman's correlation coefficient, especially in the IDH-mutant group. The highest correlation is observed in plot C, representing the correlation between ASL-CBF-high and DSC-rCBV-high, with an average Spearman's coefficient of 0.38 for IDH-mutant and 0.22 for IDH-wildtype. However, the statistical test here is insignificant (p-value > 0.05).

Significant voxel-wise correlation statistical tests are found in plots A, G, and I. Plot G, which correlates ASL-CBF low and DSC-rCBV low, shows an average Spearman's coefficient of 0.23 for IDH-mutant and 0.09 for IDH-wildtype. In contrast, plots A and I, representing the negative correlations in the mismatch regions (ASL-CBF low with DSC-rCBV high and ASL-CBF high with DSC-rCBV low, respectively), have average coefficients of -0.25 and -0.28 for IDH-mutant gliomas. For IDH-wildtype gliomas, the correlations in these regions are weaker.

Additionally, the analysis of overlapping regions in Figure 5.6 complements the findings in Figure 5.7. Particularly, the larger mismatched areas in cases of ASL-CBF low with DSC-rCBV high (plot A) and ASL-CBF high with DSC-rCBV low (plot I) in the IDH-wildtype group demonstrate a very weak correlation, suggesting distinct perfusion characteristics in these areas.

6

Discussion

This master thesis project unveils early findings on the potential correlation between arterial spin labeling cerebral blood flow (ASL-CBF) and dynamic susceptibility contrast relative cerebral blood volume (DSC-rCBV) to distinguish IDH mutation status in non-enhancing adult diffuse glioma. This master thesis project uncovers that a voxel-wise correlation between ASL-CBF and DSC-rCBV could be a valuable marker in determining IDH mutation status. Previous research on the correlation between ASL-CBF and DSC-rCBV mostly performed the correlation with the mean of intensity inside the tumor area instead of performing a voxel-wise correlation. Additionally, this master thesis project only focuses on non-enhancing glioma with very small or no blood-brain barrier (BBB) disruption, while the previous research mostly focused on enhancing glioma. In a departure from existing research, our analysis identified significantly larger mismatched areas in IDH-wildtype cases (ASL-CBF-low with DSC-rCBV-high intensity and vice versa). These areas showed no correlation between the two measures, suggesting that ASL-CBF and DSC-rCBV might capture independent physiological properties.

Given the different fields of view (FoV) and resolutions between ASL and DSC, it is important to register both images in the reference domain. The registration was done in the FLAIR domain since it has a high resolution and provides a hyperintensity area in the tumor region that does not appear in the T1-weighted image of non-enhancing gliomas. Thus, both ASL and DSC images were registered to the FLAIR domain. Furthermore, the alignments were done with the linear registration. The reason for choosing linear registration is to avoid the less robust registration due to noise and artifacts in ASL and DSC images with non-linear registration methods. Additionally, the linear registration model is simpler than non-linear registration, resulting in a faster computation.

Our evaluation of average perfusion intensity within the tumor area across different glioma types revealed that oligodendrogliomas exhibit the highest average ASL-CBF and DSC-rCBV values, followed by glioblastomas and astrocytomas, aligning with findings from other studies by Arzanforoosh et al. [8] in non enhancing glioma. Although glioblastomas are theoretically expected to have the highest microvascularization, this histological pattern does not solely reflect an increase in blood vessel number but rather an increase in proliferating endothelial and smooth muscle cells [47]. This discrepancy might explain why oligodendrogliomas show the highest ASL-CBF and DSC-rCBV values despite being IDH-mutant with characteristic branching capillaries and a "chicken wire" vascular pattern. In contrast, for IDH-wildtype, due to intense microvascular proliferation, the narrow vessel lumina in glioblastoma could account for higher ASL-CBF measurements in IDH-wild-type tumors [48], while the DSC-CBV may remain the same or slightly smaller. Thus, IDH mutation status cannot be solely determined by the average ASL-CBF or DSC-rCBV intensity.

Then, the voxelwise correlation between ASL-CBF and DSC-rCBV for the whole tumor ROI was investigated. The average of Spearman's correlation coefficient for the IDH-mutant group was higher than the IDH-wildtype counterpart, with the interclass test showing a significant difference. This result suggests that ASL-CBF and DSC-rCBV values are more similar in the IDH-mutant than the IDH-wild type.

To further analyze the difference between ASL-CBF and DSC-rCBV in distinguishing IDH mutation

status of glioma, this project divides the tumor area of ASL-CBF and DSC-rCBV into three regions: hyperperfusion, isoperfusion, and hypoperfusion. The voxelwise correlation of the hypoperfusion region for both ASL-CBF and DSC-rCBV exploits statistical significance (p-value < 0.05) in distinguishing IDH-wildtype from IDH-mutant. The overlapping area for the IDH-mutant case is higher, with a higher correlation coefficient than the IDH-wildtype, which indicates a mutual agreement between ASL-CBF and DSC-rCBV. In contrast, the IDH-wildtype group indicates a weaker correlation with a smaller overlapping area in this region, which means that the low perfusion region does not have a mutual relationship.

Further evaluation of different regions within tumors showed that IDH-wildtype tumors have larger mismatched areas than their IDH-mutant counterparts. A mismatch area means overlapping ASL-CBF-low and DSC-rCBV high or ASL-CBF-high and DSC-rCBV low. In the IDH-mutant group, mismatch areas were negatively correlated, as high and low-intensity regions are complementary. Conversely, the IDH-wildtype group displayed almost no correlation, suggesting that ASL-CBF and DSC-rCBV capture different physiological properties in these mismatch areas.

For the IDH-wildtype group, the high microvascular proliferation produces a heterogeneous vascular size. Meanwhile, for the IDH-mutant group, the vascular has a more homogenous size. These statements are also supported by Alafandi et al. [24], who found that the glioblastoma (IDH-wildtype) has more heterogenous and smaller vasculature than the IDH-mutant counterparts. This microvascular environment might be the reason for the mismatch between ASL-CBF and DSC-rCBV in the IDH-wildtype group since, with a smaller vessel, the blood flow will increase; however, the blood volume might remain the same or slightly smaller.

IDH mutations alter gliomas' metabolism, leading to slower tumor progression than tumors without such mutations. Tumors with IDH mutations (IDH-mutant) tend to exhibit lower microvascular proliferation and less dense vascularization than IDH-wildtype tumors. Additionally, in the case of IDH-wildtype, the vascular structure is highly heterogeneous. As explained in Chapter Three, physiological factors can influence the CBF and CBV values. For example - hematocrit represents the ratio of red blood cells (RBC) to the total blood volume - can affect the DSC-rCBV calculation [49]. RBC is a relatively large blood cell that tends to flow into the larger vessel; Reinhart et al. [50] support this fact, which found that the decreasing size of the vessel reduces the hematocrit value. Additionally, the research by Van Dorth et al. [33] found that the ΔR_2^* relaxation rate of DSC will increase with a higher hematocrit value, meaning that the DSC is more sensitive to larger vessels. Thus, in smaller vessels, the DSC-rCBV value could be low.

Meanwhile, for the ASL-CBF calculation, the smaller blood vessels will increase the blood flow. In addition, both ASL-CBF and DSC-rCBV have different tracers. In ASL-CBF, the tracer is a magnetically labeled water molecule. The labeled spin can be exchanged for ASL from the blood vessel to the brain parenchyma even though the BBB remains intact, resulting in ASL-CBF value. With a smaller vessel size, the probability of the water molecule spin perfuse to the brain parenchyma will increase (faster perfusion) and might cause a higher intensity of ASL-CBF. This phenomenon in the IDH-wildtype group may cause a disagreement between ASL-CBF and DSC-rCBV correlation.

ASL and DSC are different techniques to quantify perfusion value inside the brain. The quantity of ASL-CBF and DSC-rCBV are expected to be similar; this is also supported by the amount of previous research correlating the mean value of ASL-CBF and DSC-rCBV, which are highly correlated. However, the voxel-wise correlation between ASL-CBF and DSC-rCBV reveals that the correlation varies depending on the tumor region and the type of IDH mutation status. This finding can be explained based on more complex intra-tumoral microscopic interactions between IDH-mutant and IDH-wildtype. The difference in microvascular environment between IDH-mutant and IDH-wildtype glioma makes the ASL-CBF and DSC-rCBV mismatch a potential marker to differentiate IDH-mutant from IDH-wildtype noninvasively.

Limitation

One limitation of this research project is the relatively poor spatial resolution of Arterial Spin Labeling and Dynamic Susceptibility Contrast, which may not adequately capture fine details in smaller vessels, which could explain some of the discrepancies observed. The poor spatial resolution can cause a partial volume effect (PVE), where one voxel cannot represent a single brain matter. The partial volume effect from two different techniques might also result in a mismatch between ASL-CBF and DSC-rCBV. Furthermore, GRE-DSC's sensitivity to larger vessels might contribute to larger mismatch areas, as microvascular proliferation in IDH-wildtype may lead to narrower vascular lumina. Since the heterogeneous microvascular in glioblastoma, we suggest incorporating the spin echo DSC to reconstruct vessel size imaging (VSI), which may give better information than rCBV regarding the vessel size inside the tumor area. Additionally, no research currently observes the ASL-CBF value in different vessel sizes, which may help answer the different voxelwise correlation values between ASL-CBF and DSC-rCBV.

A few patients were also included for image correlation analysis, especially for the IDH-wildtype group. Since glioma with IDH-wildtype typically has an enhancing appearance, finding a non-enhancing IDH-wildtype glioma is rare. This project used a non-parametric statistical test to overcome this data imbalance between the IDH-mutant and IDH-wildtype groups. However, a larger number of patients included is important to confirm the early findings of this research project, especially for the IDH-wildtype group.

Furthermore, the analysis was limited to perfusion imaging and the confirmation of molecular status as a gold standard. It did not include a detailed assessment of histopathological features, such as vascular endothelial growth factor (VEGF), which is related to the blood vessel formation of the tumor. This limitation highlights the need for further research to evaluate the histopathological features within the mismatch area.

7

Conclusion

This study explores the capabilities of arterial spin labeling cerebral blood flow (ASL-CBF) and dynamic susceptibility contrast relative cerebral blood volume (DSC-rCBV) in identifying IDH mutation status in non-enhancing adult diffuse glioma. This research emphasizes the independent physiological properties captured by ASL-CBF and DSC-rCBV, particularly in mismatched intensity areas found predominantly in IDH-wildtype tumors, where these areas display almost no correlation between the two measures. This suggests that these imaging techniques might provide different physiological rather than similar information. This finding contradicts the previous research about the correlation between ASL and DSC, suggesting that ASL-CBF and DSC-rCBV could be equivalent; thus, ASL could be an alternative to DSC. The voxel-wise correlation between two different perfusion MRI techniques provides non-mutually exclusive image intensity, causing a lower correlation value. This research has several limitations, including no histopathological confirmation in the specific mismatch area, a small number of patients included, and poor ASL and DSC image acquisition resolution. Despite these limitations, this research offers insight into the ASL and DSC mismatch that can be a new marker for IDH mutation status confirmation with perfusion MRI.
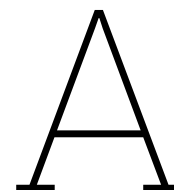
References

[1] D. N. Louis, A. Perry, G. Reifenberger, *et al.*, "The 2016 World Health Organization Classification of Tumors of the Central Nervous System: a summary," *Acta Neuropathologica*, vol. 131, no. 6, pp. 803–820, Jun. 2016, ISSN: 14320533. DOI: `10.1007/S00401-016-1545-1/TABLES/5`. [Online]. Available: `https://link.springer.com/article/10.1007/s00401-016-1545-1`.

[2] C. Horbinski, T. Berger, R. J. Packer, and P. Y. Wen, "Clinical implications of the 2021 edition of the WHO classification of central nervous system tumours," *Nature Reviews Neurology 2022 18:9*, vol. 18, no. 9, pp. 515–529, Jun. 2022, ISSN: 1759-4766. DOI: `10.1038/s41582-022-00679-w`. [Online]. Available: `https://www.nature.com/articles/s41582-022-00679-w`.

[3] A. Saaid, M. Monticelli, A. A. Ricci, *et al.*, "Prognostic Analysis of the IDH1 G105G (rs11554137) SNP in IDH-Wildtype Glioblastoma," *Genes 2022, Vol. 13, Page 1439*, vol. 13, no. 8, p. 1439, Aug. 2022, ISSN: 2073-4425. DOI: `10.3390/GENES13081439`. [Online]. Available: `https://www.mdpi.com/2073-4425/13/8/1439/htm%20https://www.mdpi.com/2073-4425/13/8/1439`.

[4] B. Sohn, C. An, D. Kim, *et al.*, "Radiomics-based prediction of multiple gene alteration incorporating mutual genetic information in glioblastoma and grade 4 astrocytoma, IDH-mutant," *Journal of Neuro-Oncology*, vol. 155, pp. 267–276, 2021. DOI: `10.1007/s11060-021-03870-z`. [Online]. Available: `https://doi.org/10.1007/s11060-021-03870-z`.

[5] G. Zhang, X. Xu, L. Zhu, *et al.*, "A Novel Molecular Classification Method for Glioblastoma Based on Tumor Cell Differentiation Trajectories," *Stem Cells International*, vol. 2023, 2023, ISSN: 16879678. DOI: `10.1155/2023/2826815`.

[6] A. L. Cohen, S. L. Holmen, and H. Colman, "NEURO-ONCOLOGY (LE ABREY, SECTION EDITOR) IDH1 and IDH2 Mutations in Gliomas," *Current Neurology and Neuroscience Reports*, vol. 13, 2013. DOI: `10.1007/s11910-013-0345-4`.

[7] M. Dijsselhof, B. E. Padrela, J. Petr, and H. J. Mutsaerts, "Arterial spin labeling MRI," in *Quantitative Perfusion MRI: Techniques, Applications and Practical Considerations*, vol. 11, Academic Press, Jan. 2023, pp. 77–107. DOI: `10.1016/B978-0-323-95209-5.00007-6`.

[8] F. Arzanforoosh, S. R. van der Voort, F. Incekara, *et al.*, "Microvasculature Features Derived from Hybrid EPI MRI in Non-Enhancing Adult-Type Diffuse Glioma Subtypes," *Cancers 2023, Vol. 15, Page 2135*, vol. 15, no. 7, p. 2135, Apr. 2023, ISSN: 2072-6694. DOI: `10.3390/CANCERS15072135`. [Online]. Available: `https://www.mdpi.com/2072-6694/15/7/2135/htm%20https://www.mdpi.com/2072-6694/15/7/2135`.

[9] P. Kickingereder, B. Wiestler, F. Sahm, *et al.*, "Primary central nervous system lymphoma and atypical glioblastoma: Multiparametric differentiation by using diffusion-, perfusion-, and susceptibility-weighted MR imaging," *Radiology*, vol. 272, no. 3, pp. 843–850, May 2014, ISSN: 15271315. DOI: `10.1148/RADIOL.14132740/ASSET/IMAGES/LARGE/RADIOL.14132740.FIG3D.JPEG`. [Online]. Available: `https://pubs.rsna.org/doi/10.1148/radiol.14132740`.

[10] A. Lasocki, F. Gaillard, X. A. Lasocki, and X. F. Gaillard, "Non-Contrast-Enhancing Tumor: A New Frontier in Glioblastoma Research," *American Journal of Neuroradiology*, vol. 40, no. 5, pp. 758–765, May 2019, ISSN: 0195-6108. DOI: `10.3174/AJNR.A6025`. [Online]. Available: `https://www.ajnr.org/content/40/5/758%20https://www.ajnr.org/content/40/5/758.abstract`.

[11] D. A. Hardesty and N. Sanai, "The value of glioma extent of resection in the modern neurosurgical era," *Frontiers in Neurology*, vol. OCT, p. 33 329, Oct. 2012, ISSN: 16642295. DOI: `10.3389/FNEUR.2012.00140/BIBTEX`. [Online]. Available: `www.frontiersin.org`.

[12] M. Lacroix, D. Abi-Said, D. R. Fourney, *et al.*, "A multivariate analysis of 416 patients with glioblastoma multiforme: prognosis, extent of resection, and survival," *Journal of neurosurgery*, vol. 95, no. 2, pp. 190–198, 2001, ISSN: 0022-3085. DOI: `10.3171/JNS.2001.95.2.0190`. [Online]. Available: `https://pubmed.ncbi.nlm.nih.gov/11780887/`.

[13] M. Garrett, Y. Fujii, N. Osaka, D. Ito, Y. Hirota, and A. T. Sasaki, "Emerging Roles of Wild-type and Mutant IDH1 in Growth, Metabolism and Therapeutics of Glioma," *Gliomas*, pp. 61–78, May 2021. DOI: `10.36255/EXONPUBLICATIONS.GLIOMAS.2021.CHAPTER4`. [Online]. Available: `https://pubmed.ncbi.nlm.nih.gov/34038049/`.

[14] S. Iqbal, M. U. G. Khan, T. Saba, and A. Rehman, "Computer-assisted brain tumor type discrimination using magnetic resonance imaging features," *Biomedical Engineering Letters*, vol. 8, no. 1, pp. 5–28, Feb. 2018, ISSN: 2093985X. DOI: `10.1007/S13534-017-0050-3/TABLES/7`. [Online]. Available: `https://link.springer.com/article/10.1007/s13534-017-0050-3`.

[15] M. Hameurlaine and A. Moussaoui, "Survey of Brain Tumor Segmentation Techniques on Magnetic Resonance Imaging," *Nano Biomedicine and Engineering*, vol. 11, no. 2, pp. 178–191, 2019, ISSN: 2097-3837. DOI: `10.5101/NBE.V11I2.P178-191`. [Online]. Available: `https://www.sciopen.com/article/10.5101/nbe.v11i2.p178-191`.

[16] Y. W. Park, P. Vollmuth, M. Foltyn-Dumitru, *et al.*, "The 2021 WHO Classification for Gliomas and Implications on Imaging Diagnosis: Part 1—Key Points of the Fifth Edition and Summary of Imaging Findings on Adult-Type Diffuse Gliomas," *Journal of Magnetic Resonance Imaging*, vol. 58, no. 3, pp. 677–689, Sep. 2023, ISSN: 1522-2586. DOI: `10.1002/JMRI.28743`. [Online]. Available: `https://onlinelibrary.wiley.com/doi/full/10.1002/jmri.28743%20https://onlinelibrary.wiley.com/doi/abs/10.1002/jmri.28743%20https://onlinelibrary.wiley.com/doi/10.1002/jmri.28743`.

[17] A. Perry and P. Wesseling, "Histologic classification of gliomas," *Handbook of Clinical Neurology*, vol. 134, pp. 71–95, Jan. 2016, ISSN: 0072-9752. DOI: `10.1016/B978-0-12-802997-8.00005-0`.

[18] W. Wang, Y. Zhao, L. Teng, *et al.*, "Neuropathologist-level integrated classification of adult-type diffuse gliomas using deep learning from whole-slide pathological images," *Nature Communications 2023 14:1*, vol. 14, no. 1, pp. 1–11, Oct. 2023, ISSN: 2041-1723. DOI: `10.1038/s41467-023-41195-9`. [Online]. Available: `https://www.nature.com/articles/s41467-023-41195-9`.

[19] J. H. Rees, "Oligodendrogliomas," *Blue Books of Neurology*, vol. 36, pp. 132–149, Jan. 2010, ISSN: 1877-184X. DOI: `10.1016/B978-0-7506-7516-1.00007-4`.

[20] I. C. Hvinden, T. Cadoux-Hudson, C. J. Schofield, and J. S. O. Mccullagh, "Metabolic adaptations in cancers expressing isocitrate dehydrogenase mutations," *Cell Reports Medicine*, vol. 2, p. 100 469, 2021. DOI: `10.1016/j.xcrm.2021.100469`. [Online]. Available: `https://doi.org/10.1016/j.xcrm.2021.100469`.

[21] T. Sugahara, Y. Korogi, M. Kochi, *et al.*, "Correlation of MR imaging-determined cerebral blood volume maps with histologic and angiographic determination of vascularity of gliomas.," *https://doi.org/10.2214/ajr.171* vol. 171, no. 6, pp. 1479–1486, Jan. 2013, ISSN: 0361803X. DOI: `10.2214/AJR.171.6.9843274`. [Online]. Available: `https://www.ajronline.org/doi/10.2214/ajr.171.6.9843274`.

[22] E. A. Knopp, S. Cha, G. Johnson, *et al.*, "Glial neoplasms: Dynamic contrast-enhanced T2*-weighted MR imaging," *Radiology*, vol. 211, no. 3, pp. 791–798, Jun. 1999, ISSN: 00338419. DOI: `10.1148/RADIOLOGY.211.3.R99JN46791/ASSET/IMAGES/LARGE/R99JN46C6B.JPEG`. [Online]. Available: `https://pubs.rsna.org/doi/10.1148/radiology.211.3.r99jn46791`.

[23] J. M. Abrigo, D. M. Fountain, J. M. Provenzale, *et al.*, "Magnetic resonance perfusion for differentiating low-grade from high-grade gliomas at first presentation," *Cochrane Database of Systematic Reviews*, vol. 2018, no. 1, Jan. 2018, ISSN: 14651858. DOI: `10.1002/14651858.CD011551.PUB2/MEDIA/CDSR/CD011551/IMAGE{\_}N/NCD011551-TST-001.PNG`. [Online]. Available: `https://www.cochranelibrary.com/cdsr/doi/10.1002/14651858.CD011551.pub2/full%20https://www.cochranelibrary.com/cdsr/doi/10.1002/14651858.CD011551.pub2/abstract`.

[24] A. Alafandi, S. S. Tbalvandany, F. Arzanforoosh, *et al.*, "Probing the glioma microvasculature: a case series of the comparison between perfusion MRI and intraoperative high-frame-rate ultrafast Doppler ultrasound," *European Radiology Experimental*, vol. 8, no. 1, pp. 1–12, Dec. 2024, ISSN: 25099280. DOI: `10.1186/S41747-023-00406-0/FIGURES/8`. [Online]. Available: `https://eurradiolexp.springeropen.com/articles/10.1186/s41747-023-00406-0`.

[25] R. H. Hashemi, W. G. Bradley Jr, and C. J. Lisanti, *MRI: The Basics*. Wolters Kluwer, 2017, vol. IV.

[26] E. Grøvik, A. Bjørnerud, and K. E. Emblem, "Dynamic Susceptibility Contrast MRI: Basic Physics, Pulse Sequences, and Modeling," in *Advances in Magnetic Resonance Technology and Applications*, vol. 1, Academic Press, Jan. 2020, pp. 345–367. DOI: `10.1016/B978-0-12-817057-1.00016-0`.

[27] J. L. Boxerman, C. C. Quarles, L. S. Hu, *et al.*, "Consensus recommendations for a dynamic susceptibility contrast MRI protocol for use in high-grade gliomas," *Neuro-Oncology*, vol. 22, no. 9, pp. 1262–1275, Sep. 2020, ISSN: 1522-8517. DOI: `10.1093/NEUONC/NOAA141`. [Online]. Available: `https://dx.doi.org/10.1093/neuonc/noaa141`.

[28] K. Welker, J. Boxerman, A. Kalnin, T. Kaufmann, M. Shiroishi, and M. Wintermark, "ASFNR Recommendations for Clinical Performance of MR Dynamic Susceptibility Contrast Perfusion Imaging of the Brain," *American Journal of Neuroradiology*, vol. 36, no. 6, E41–E51, Jun. 2015, ISSN: 0195-6108. DOI: `10.3174/AJNR.A4341`. [Online]. Available: `https://www.ajnr.org/content/36/6/E41%20https://www.ajnr.org/content/36/6/E41.abstract`.

[29] A. Chakravorty, T. Steel, and J. Chaganti, "Accuracy of percentage of signal intensity recovery and relative cerebral blood volume derived from dynamic susceptibility-weighted, contrast-enhanced MRI in the preoperative diagnosis of cerebral tumours," *https://doi.org/10.1177/1971400915611916*, vol. 28, no. 6, pp. 574–583, Oct. 2015, ISSN: 23851996. DOI: `10.1177/1971400915611916`. [Online]. Available: `https://journals.sagepub.com/doi/10.1177/1971400915611916`.

[30] L. Axel, "Cerebral blood flow determination by rapid-sequence computed tomography: theoretical analysis.," *https://doi.org/10.1148/radiology.137.3.7003648*, vol. 137, no. 3, pp. 679–686, Dec. 1980, ISSN: 00338419. DOI: `10.1148/RADIOLOGY.137.3.7003648`. [Online]. Available: `https://pubs.rsna.org/doi/10.1148/radiology.137.3.7003648`.

[31] C. Lorenz, T. Benner, P. J. Chen, *et al.*, "Automated perfusion-weighted MRI using localized arterial input functions," *Journal of Magnetic Resonance Imaging*, vol. 24, no. 5, pp. 1133–1139, Nov. 2006, ISSN: 10531807. DOI: `10.1002/JMRI.20717`.

[32] G. N. Stewart, "Researches on the Circulation Time in Organs and on the Influences which affect it: Parts I.—III.," *The Journal of Physiology*, vol. 15, no. 1-2, pp. 1–89, Jul. 1893, ISSN: 14697793. DOI: `10.1113/JPHYSIOL.1893.SP000462`.

[33] D. van Dorth, K. Venugopal, D. H. Poot, *et al.*, "Dependency of R2 and R2* relaxation on Gd-DTPA concentration in arterial blood: Influence of hematocrit and magnetic field strength," *NMR in Biomedicine*, vol. 35, no. 5, e4653, May 2022, ISSN: 1099-1492. DOI: `10.1002/NBM.4653`. [Online]. Available: `https://onlinelibrary.wiley.com/doi/full/10.1002/nbm.4653%20https://onlinelibrary.wiley.com/doi/abs/10.1002/nbm.4653%20https://analyticalsciencejournals.onlinelibrary.wiley.com/doi/10.1002/nbm.4653`.

[34] J. A. Detre, J. S. Leigh, D. S. Williams, and A. P. Koretsky, "Perfusion imaging," *Magnetic Resonance in Medicine*, vol. 23, no. 1, pp. 37–45, Jan. 1992, ISSN: 1522-2594. DOI: `10.1002/MRM.1910230106`. [Online]. Available: `https://onlinelibrary.wiley.com/doi/full/10.1002/mrm.1910230106%20https://onlinelibrary.wiley.com/doi/abs/10.1002/mrm.1910230106%20https://onlinelibrary.wiley.com/doi/10.1002/mrm.1910230106`.

[35] W. C. Wu, M. Fernández-Seara, J. A. Detre, F. W. Wehrli, and J. Wang, "A theoretical and experimental investigation of the tagging efficiency of pseudocontinuous arterial spin labeling," *Magnetic Resonance in Medicine*, vol. 58, no. 5, pp. 1020–1027, Nov. 2007, ISSN: 1522-2594. DOI: `10.1002/MRM.21403`. [Online]. Available: `https://onlinelibrary.wiley.com/doi/full/10.1002/mrm.21403%20https://onlinelibrary.wiley.com/doi/abs/10.1002/mrm.21403%20https://onlinelibrary.wiley.com/doi/10.1002/mrm.21403`.

[36] H. M. Gach and W. Dai, "Simple model of double adiabatic inversion (DAI) efficiency," *Magnetic resonance in medicine*, vol. 52, no. 4, pp. 941–946, 2004, ISSN: 0740-3194. DOI: `10.1002/MRM.20240`. [Online]. Available: `https://pubmed.ncbi.nlm.nih.gov/15389933/`.

[37] D. C. Alsop, J. A. Detre, X. Golay, *et al.*, "Recommended implementation of arterial spin-labeled perfusion MRI for clinical applications: A consensus of the ISMRM perfusion study group and the European consortium for ASL in dementia," *Magnetic resonance in medicine*, vol. 73, no. 1, pp. 102–116, Jan. 2015, ISSN: 1522-2594. DOI: `10.1002/MRM.25197`. [Online]. Available: `https://pubmed.ncbi.nlm.nih.gov/24715426/`.

[38] M. Smits, "MRI biomarkers in neuro-oncology," *Nature Reviews Neurology 2021 17:8*, vol. 17, no. 8, pp. 486–500, Jun. 2021, ISSN: 1759-4766. DOI: `10.1038/s41582-021-00510-y`. [Online]. Available: `https://www.nature.com/articles/s41582-021-00510-y`.

[39] D. Khashbat, T. Abe, M. Ganbold, *et al.*, "Correlation of 3D Arterial Spin Labeling and Multi-Parametric Dynamic Susceptibility Contrast Perfusion MRI in Brain Tumors," *The journal of medical investigation : JMI*, vol. 63, no. 3-4, pp. 175–181, 2016, ISSN: 1349-6867. DOI: `10.2152/JMI.63.175`. [Online]. Available: `https://pubmed.ncbi.nlm.nih.gov/27644554/`.

[40] A. Lavrova, W. Teunissen, E. Warnert, M. Bent, and M. Smits, "Diagnostic Accuracy of Arterial Spin Labeling in Comparison With Dynamic Susceptibility Contrast-Enhanced Perfusion for Brain Tumor Surveillance at 3T MRI," *Frontiers in Oncology*, vol. 12, 2022.

[41] T. Hashido and S. Saito, "A radiomics-based comparative study on arterial spin labeling and dynamic susceptibility contrast perfusion-weighted imaging in gliomas," *Nature Scientific Reports*, 2020. DOI: `10.1038/s41598-020-62658-9`. [Online]. Available: `https://doi.org/10.1038/s41598-020-62658-9`.

[42] H. Park, J. Lee, S. H. Park, and S. H. Choi, "Evaluation of Tumor Blood Flow Using Alternate Ascending/Descending Directional Navigation in Primary Brain Tumors: A Comparison Study with Dynamic Susceptibility Contrast Magnetic Resonance Imaging," *Korean Journal of Radiology*, vol. 20, no. 2, pp. 275–282, Feb. 2019, ISSN: 1229-6929. DOI: `10.3348/KJR.2018.0300`. [Online]. Available: `https://doi.org/10.3348/kjr.2018.0300`.

[43] M. Van Der Thiel, C. Rodriguez, P. Giannakopoulos, *et al.*, "Brain Perfusion Measurements Using Multidelay Arterial Spin-Labeling Are Systematically Biased by the Number of Delays," *AJNR: American Journal of Neuroradiology*, vol. 39, no. 8, p. 1432, Aug. 2018, ISSN: 1936959X. DOI: `10.3174/AJNR.A5717`. [Online]. Available: `/pmc/articles/PMC7410552/%20/pmc/articles/PMC7410552/?report=abstract%20https://www.ncbi.nlm.nih.gov/pmc/articles/PMC7410552/`.

[44] *FLIRT/UserGuide - FslWiki*. [Online]. Available: `https://fsl.fmrib.ox.ac.uk/fsl/fslwiki/FLIRT/UserGuide`.

[45] M. J. Van Osch, W. M. Teeuwisse, M. A. Van Walderveen, J. Hendrikse, D. A. Kies, and M. A. Van Buchem, "Can arterial spin labeling detect white matter perfusion signal?" *Magnetic Resonance in Medicine*, vol. 62, no. 1, pp. 165–173, Jul. 2009, ISSN: 1522-2594. DOI: `10.1002/MRM.22002`. [Online]. Available: `https://onlinelibrary.wiley.com/doi/full/10.1002/mrm.22002%20https://onlinelibrary.wiley.com/doi/abs/10.1002/mrm.22002%20https://onlinelibrary.wiley.com/doi/10.1002/mrm.22002`.

[46] Y. Zhang, M. Brady, and S. Smith, "Segmentation of brain MR images through a hidden Markov random field model and the expectation-maximization algorithm," *IEEE transactions on medical imaging*, vol. 20, no. 1, pp. 45–57, Jan. 2001, ISSN: 0278-0062. DOI: `10.1109/42.906424`. [Online]. Available: `https://pubmed.ncbi.nlm.nih.gov/11293691/`.

[47] J. Zhou, N. Li, G. Yang, and Y. Zhu, "Vascular patterns of brain tumors," *International Journal of Surgical Pathology*, vol. 19, no. 6, pp. 709–717, Dec. 2011, ISSN: 10668969. DOI: `10.1177/1066896911417710/ASSET/IMAGES/LARGE/10.1177{\_}1066896911417710-FIG3.JPEG`. [Online]. Available: `https://journals.sagepub.com/doi/10.1177/1066896911417710`.

[48] P. A. Stewart, C. L. Farrell, and R. F. Del Maestro, "The effect of cellular microenvironment on vessels in the brain. Part 1: Vessel structure in tumour, peritumour and brain from humans with malignant glioma," *International Journal of Radiation Biology*, vol. 60, no. 1-2, pp. 125–130, 1991, ISSN: 09553002. DOI: `10.1080/09553009114551701/ASSET//CMS/ASSET/7721211F-0D2C-47FF-93ED-ADC02422C327/09553009114551701.FP.PNG`. [Online]. Available: `https://www.tandfonline.com/doi/abs/10.1080/09553009114551701`.

[49] C. C. Quarles and P. Choudhary, "Dynamic susceptibility contrast MRI," vol. 11, pp. 41–75, Jan. 2023, ISSN: 2666-9099. DOI: `10.1016/B978-0-323-95209-5.00001-5`.

[50] W. H. Reinhart, N. Z. Piety, and S. S. Shevkoplyas, "Influence of feeding hematocrit and perfusion pressure on hematocrit reduction (Fåhræus effect) in an artificial microvascular network," *Microcirculation*, vol. 24, no. 8, e12396, Nov. 2017, ISSN: 1549-8719. DOI: `10.1111/MICC.12396`. [Online]. Available: `https://onlinelibrary.wiley.com/doi/full/10.1111/micc.12396%20https://onlinelibrary.wiley.com/doi/abs/10.1111/micc.12396%20https://onlinelibrary.wiley.com/doi/10.1111/micc.12396`.

A

Additional Tables and Charts

A.1. Average Percentage of Overlapping Region

Table A.1 and table A.2 show the average percentage of overlapping ASL-CBF and DSC-rCBV in IDH-mutant and IDH-wildtype consecutively. As depicted in both tables, the DSC-high and ASL-high average percentage overlapping area difference between IDH-mutant and IDH-wildtype is quite large. However, the statistical test shows that the difference between IDH-mutant and IDH-wildtype overlapping regions is insignificant in this region.

Average Percentage of Overlapping Region IDH- Mutant			
	DSC-LOW	DSC-MEDIUM	DSC-HIGH
ASL-HIGH	4.66*	9.11	17.63
ASL-MEDIUM	11.45	13.69	10.52
ASL-LOW	16.05*	10.34	4.01*

Table A.1: Average Percentage of Overlapping Region IDH- Mutant. Values with asterisks represent significant differences between IDH-mutant and IDH-wildtype.

Average Percentage of Overlapping Region IDH-Wildtype			
	DSC-LOW	DSC-MEDIUM	DSC-HIGH
ASL-HIGH	7.2*	9.02	14.23
ASL-MEDIUM	12.66	14.15	10.67
ASL-LOW	12.51*	10.18	7.47*

Table A.2: Average Percentage of Overlapping Region IDH-Wildtype. Values with asterisks represent significant differences between IDH-mutant and IDH-wildtype.

A.2. Average Spearman's Correlation Coefficient

Similar to the percentage overalaping region, the Spearman's correlation coefficient are also only significant in three cases: ASL-CBF-High with DSC-rCBV-Low, ASL-CBF-Low with DSC-rCBV-low, and ASL CBF-Low and DSC-rCBV-high.

Average Spearman's Coefficient Correlation IDH- Mutant			
	DSC-LOW	**DSC-MEDIUM**	**DSC-HIGH**
ASL-HIGH	-0.25*	-0.06	0.38
ASL-MEDIUM	-0.02	0.07	-0.04
ASL-LOW	0.23*	-0.01	-0.28*

Table A.3: Average Spearman's Coefficient Correlation IDH- Mutant. Values with asterisks represent significant differences between IDH-mutant and IDH-wildtype.

Average Spearman's Coefficient Correlation IDH- wildtype			
	DSC-LOW	**DSC-MEDIUM**	**DSC-HIGH**
ASL-HIGH	-0.13	-0.06	0.22
ASL-MEDIUM	0.01	0.06	-0.07
ASL-LOW	0.09	0	-0.12

Table A.4: Average Spearman's Coefficient Correlation IDH- wildtype. Values with asterisks represent significant differences between IDH-mutant and IDH-wildtype.

B

Additional Images

These images show the ASL-CBF and DSC-rCBV being overlayed on top of FLAIR images. Figure B.1, B.2, B.3 were the perfusion values from patients with Oligodendroglioma (IDH-mutant), Astrocytoma (IDH-mutant), Glioblastoma (IDH-wildtype) consecutively. Those three images show that the IDH-wildtype case has a larger mismatch area than the IDH-mutant case.
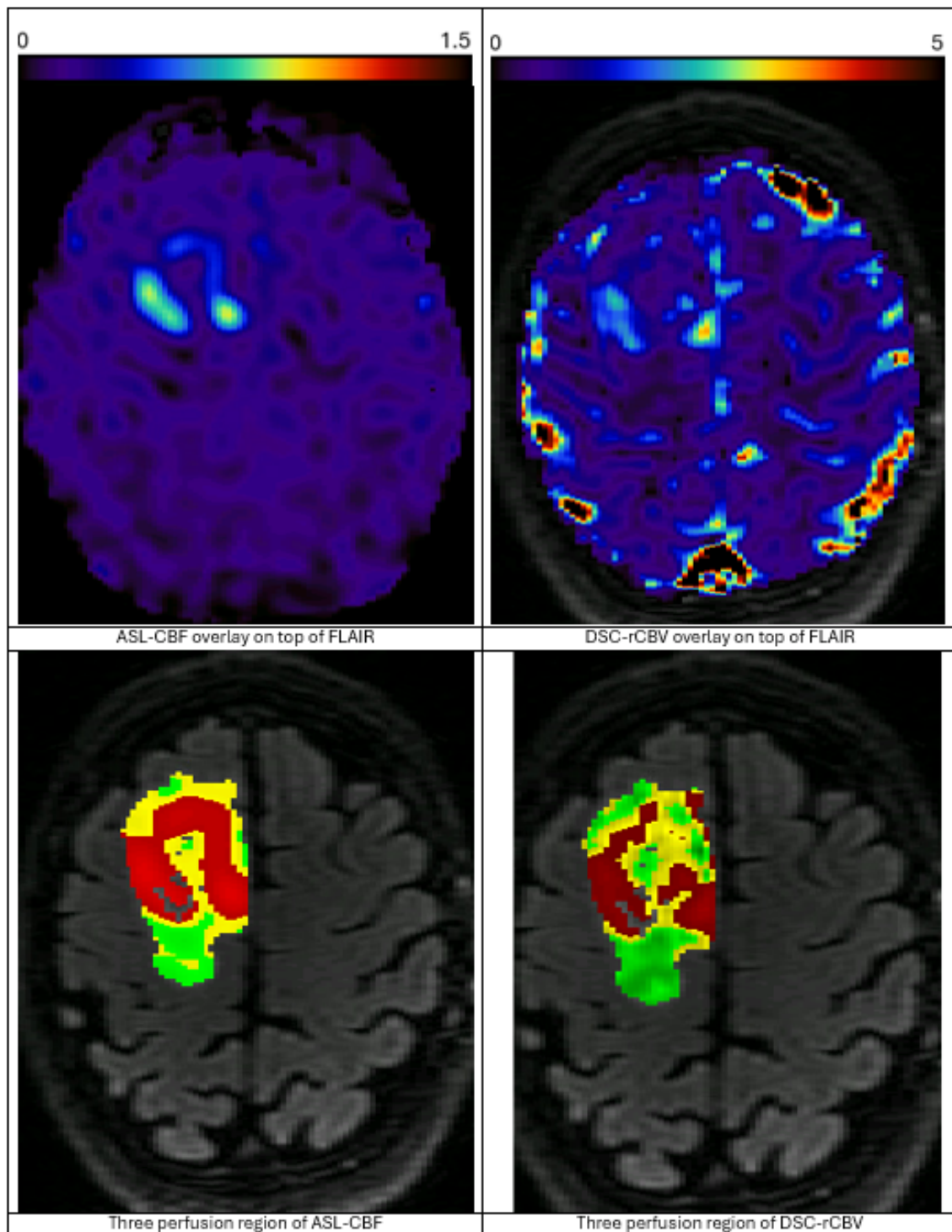
Figure B.1: Patient-01 Oligodendroglioma IDH-mutant. The left column represents ASL-CBF, and the right column represents DSC-rCBV. The top row depicts the perfusion value in the patient's whole brain, while the bottom row depicts the three different perfusion regions inside tumor ROI. For the bottom row, red = high perfusion, yellow = medium perfusion, and green = low perfusion. From the top row images, oligodendroglioma has a high perfusion value for both ASL-CBF and DSC inside the tumor region.
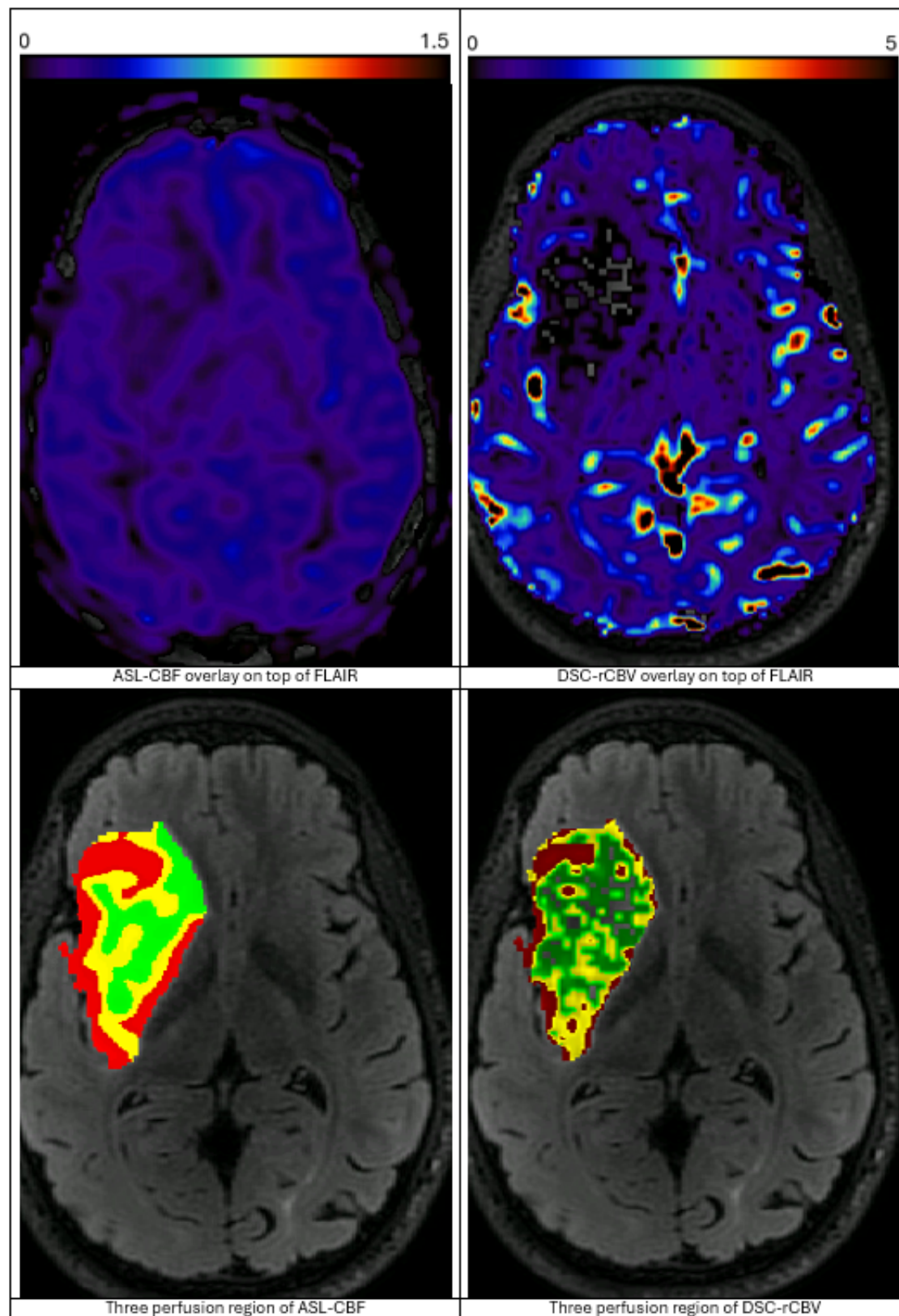
Figure B.2: Patient-08 Astrocytoma IDH-mutant. The left column represents ASL-CBF, and the right column represents DSC-rCBV. The top row depicts the perfusion value in the patient's whole brain, while the bottom row depicts the three different perfusion regions inside tumor ROI. For the bottom row, red = high perfusion, yellow = medium perfusion, and green = low perfusion. From the top row images, astrocytoma has a lower perfusion value for both ASL-CBF and DSC inside the tumor region compared to the contralateral region.
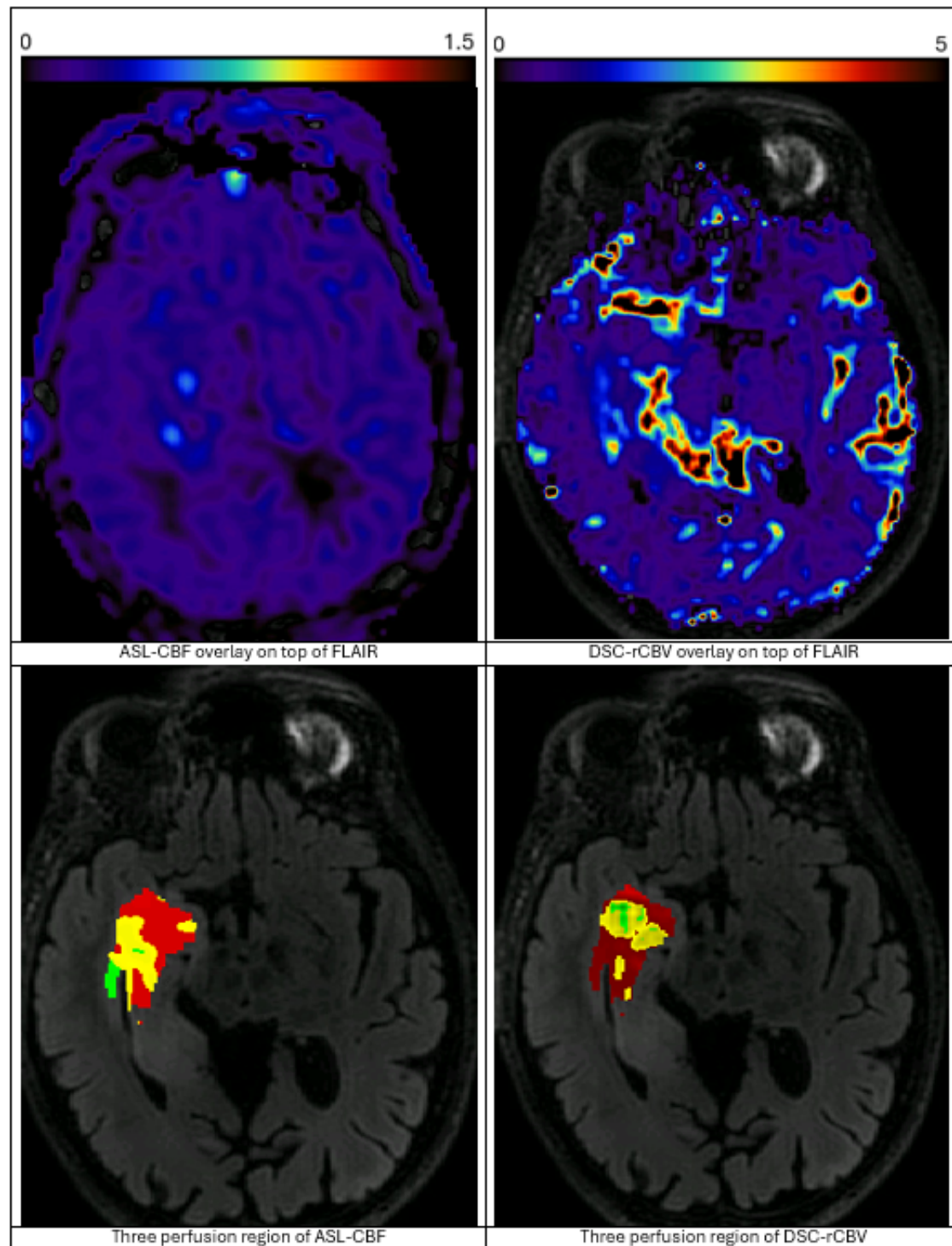
Figure B.3: Patient-17 Glioblastoma IDH-wildtype. The left column represents ASL-CBF, and the right column represents DSC-rCBV. The top row depicts the perfusion value in the patient's whole brain, while the bottom row depicts the three different perfusion regions inside tumor ROI. For the bottom row, red = high perfusion, yellow = medium perfusion, and green = low perfusion.

C
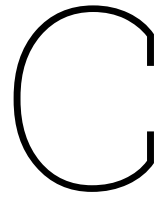
Source Code

The source code for this thesis project is available on GitHub (`https://github.com/ahmadhabbie/MasterThesis`)